Computational Fluid Dynamics Modeling of Flashing Flow in Convergent-Divergent Nozzle

Quang Dang Le[1], Riccardo Mereu, Giorgio Besagni, Vincenzo Dossena, Fabio Inzoli

Department of Energy, Politecnico di Milano, via Lambruschini 4, Milan 20156, Italy

In this paper, a computational fluid dynamics model of flashing flow, which considers the thermal nonequilibrium effect, has been proposed. In the proposed model, based on the two-phase mixture approach, the phase-change process depends on the difference between the vaporization pressure and the vapor partial pressure. The thermal nonequili-brium effect has been included by using ad hoc modeling of the boiling delay. The proposed model has been applied to the case of two-dimensional axisymmetric convergent-divergent nozzle, which is representative of well-known applications in nuclear and energy engineering applications (e.g., the primary flow in the motive nozzle of ejectors). The numerical results have been validated based on a benchmark case from the literature and have been compared with the numerical results previously obtained by different research groups. The proposed approach has shown a good level of agreement as regards the global and the local experimental fluid dynamic quantities. In addition, sensitivity analyses have been carried out concerning (a) grid independency, (b) turbu-lence modeling approaches, (c) near-wall treatment approaches, (d) turbulence inlet parameters, and (e) semi-empirical coefficients. In conclusion, the present paper aims to provide guidelines for the simulation of flash boiling flow in industrial applications.

Keywords: flash boiling, CFD, nozzle, multiphase flow, nonequilibrium effects, validation

1 Introduction

Flashing flow is a phase change phenomenon, which occurs in high-speed flow inside nozzles, because of the thermal nonequilibrium effect (viz. the boiling delay phenomenon) [1,2]. Flashing flow is of practical interest in industrial applications; a typical example concerns the high-speed flows in the primary nozzle of ejectors: the correct prediction of this contribution is requested to correctly design ejector-based systems. In the last decades, owing to the practical importance of the flashing phenomenon, many studies have been proposed concerning both theoretical approaches [1–5] and experimental studies [6–9]. In particular, there is a growing attention toward computational fluid dynamics (CFD) to predict the global and local fluid dynamic quantities, thus improving the understanding of the physical behavior inside the nozzle. Among the different approaches, the homogeneous equilibrium model (HEM) is generally recognized as the simplest one (see Ref. [3]). Within this approach, the flashing flow is considered as pseudo single-phase flowing through the nozzle at the equilibrium state. The HEM approach can be applied to relatively long nozzles, which allow for a smooth phase change inside them; conversely, the application of the HEM approach in short nozzles can result in large errors, as the equilibrium assumption is no longer valid. To overcome these limitations, nonequilibrium effects have been included by using nonequilibrium models, which may concern (a) empirical correction factors (see Ref. [10]), (b) slip between phases (i.e., mixture models), and (c) two-fluid models [11–13]. Unfortunately, an important drawback is that usually the needed closure models (i.e., flow pattern details, information about bubble size distributions and bubble shapes) are selected on a case-by-case basis, which hinder improvement of the predictive value.

In general, CFD approaches to model flashing flows must consider the following two aspects: (a) the change of phase during flashing flow and (b) the interaction between the liquid phase and the vapor phase during the vaporization process. Both these aspects are briefly described hereunder. Concerning the change of phase during flashing flow, the models can be classified into two main categories: (a) models accounting for the nucleation process, which generally show better agreement with the real fluid-flow behavior, but require experimental data to tune the source term of the nucleation equation (refer to Table 1) and (b) models neglecting the nucleation process and assuming constant bubble size or number density, with artificial coefficients to control the nonequilibrium effects (refer to Table 2). Concerning the interaction between the liquid phase and the vapor phase during the vaporization process, two approaches are commonly used: (i) the Euler-multi-fluid approach and (ii) the mixture approach. Within the Eulerian multi-fluid approach, the conservation equations are phase-averaged and the turbulence for large-scale simulations is usually described by the corresponding Reynolds-averaged Navier–Stokes (RANS) equations. The interaction between the phases has to be taken into account by interfacial exchange terms. Such exchange terms, usually denoted as closures, have to include: (i) the exchange of momentum between the liquid and

[1]Corresponding author.

Contributed by the Fluids Engineering Division of ASME for publication in the Journal of Fluids Engineering. Manuscript received March 20, 2017; final manuscript received April 2, 2018; published online May 7, 2018. Assoc. Editor: Ioannis K. Nikolos.

e-mail: lequang.dang@polimi.it, riccardo.mereu@polimi.it, giorgio.besagni@polimi.it, vincenzo.dossena@polimi.it, fabio.inzoli@polimi.it

Table 1 Flashing flow simulation using nucleation models: a literature survey

References and code	Numerical model and assumptions	Experimental benchmark and remarks
[14]–CFX 4.2	– Euler–Euler model Scalar transport equation for bubble number density with wall nucleation as source term. – Nucleation rate is determined by model of Jones [15–18]. – Mean bubble diameter and interfacial area density are determined by void fraction and bubble number density. – Mass, energy, and momentum transfer driven by nucleation are not considered. – Dominated conduction at interface. – Vapor is kept at saturated state through process.	– Flashing flows in pipes and nozzles [8]. – Relative motion of bubbles leads to dominant convective heat transfer in most cases of flashing flow.
[19]–FLUENT 6.2.16	– Euler–Euler model. – Considering effects of bubble nucleation and interfacial heat transfer to phase change process, momentum, and energy conservation. – Lift, wall lubrication, and turbulent dispersion forces are ignored in momentum transfer. – A transport equation for bubbles with only source term of heterogeneous nucleation. – Model for nucleation is modified from study of Ref. [20] using two unphysical parameters to improve stability of model.	– A piping system to connect two flashing tanks at Rusal Aughinish. Flashing phenomenon is accounted in depressurization process. – Around 5% of error between numerical results and estimated plant flows.
[21] NEPTUNE-CFD	– Euler–Euler model. – Using unphysical heat transfer coefficient. – Interphase momentum transfers in this model consist of drag, added mass, and lift forces. – Nucleation effects to vapor generation rate, momentum, and energy transfer is performed by modified version of Jones' model [15–18]. – Saturated vapor phase is kept for entire process.	– Critical flow in nozzle [22] with initially subcooled inlet and flashing outlet. To capture correctly radial vapor profile, model requires experimental information. – Experimental test from Ref. [23] with cavitation developments downstream an orifice. There is an agreement qualitatively between numerical results and experimental visualizations.
[24] CFX 14.5	– Euler. – Euler model (Saturation stage is kept for vapor phase so model does not require energy balance at vapor phase). – Interphase momentum transfer includes drag, lift, lubrication, virtual mass, and turbulent dispersion force. – Interphase mass transfer depends on interfacial heat transfer. – Bubble number density is solved by bubble number transport equation focusing on nucleation, the effect of coalescence only, and neglecting break-up process of bubble. – Testing nucleation models applying to bubble number transport equation from Ref. [18] Rensselaer Polytechnic Institute (RPI) model [25–27], Riznic model [28,29], and Rohatgi model [30]. – Reducing number of bubbles due to coalescence effect is proportional to the bubble number density.	– Vertical circular convergent-divergent nozzle from Ref. [31]. There is good agreement with experiment in terms of critical flow rate and axial profiles but radial vapor fraction is not satisfied.
[32] STAR-CD	– Mixture model with barotropic phase change. – Rayleigh-Plesset equation for the bubble growth. – Including surface tension in momentum equation.	– A single-hole diesel injector with different needle's lifts. – For case of fully open injector, there is an agreement in term of discharge coefficient between numerical result and experiment with maximum error of 1.3%.

gas phases, (ii) the effects of the dispersed bubbles on the turbulence of the continuous phase, and (iii) processes of bubble coalescence and break-up that determine the bubble size distribution. Unfortunately, the closure relations used to couple the phases rely on experimental data, rarely available for practical applications [47]. Conversely, the mixture model assumes that individual components in multiphase flow move at the same velocity over short length scales (viz., homogeneous flow). This assumption is suitable for drag-dominated multiphase flows, with strong coupling between the two phases [47]. In the mixture model, a single momentum equation is considered to infer the average velocity field of the mixture flow. Volume fraction is, thus, extracted by solving the individual continuity equation for each of the phases. When gravity and centrifugal forces become more significant, relative motion between two phases appears and must be considered in the mixture model. There are several models for velocity differences between two phases, including: the drift-flux model [48], the mixture model [11], the algebraic-slip model [49], the suspension approach [50], the diffusion model [11,51], and the local-equilibrium model [52].

Taking into account the above-mentioned literature survey (see Tables 1 and 2), this paper contributes to the existing discussion

Table 2 Flashing flow simulation neglecting nucleation process

References and code	Numerical model and assumptions	Experimental benchmark and remarks
Laurien and colleagues [33–35] CFX 4.2	– Euler–Euler model. – Momentum transfer only considers drag force and neglecting nondrag forces. – Allowing growth of bubble size by assuming bubble number density. – Vapor phase is always kept at saturation state.	– Cavitation flow in pipes. – With growth of bubble size, model is closer to physical behaviors of flow boiling. – Assumptions of model are only reasonable with narrow nucleation zone.
[36] CFX	– Euler–Euler model. – Only considering drag force for momentum transfer. – Bubble diameter is assumed constant (1 mm). – Always saturation state for vapor phase.	– Edward blowdown test.
[37] CFX 14.0	– Euler–Euler model (Saturation stage is kept for vapor phase so model does not require energy balance at vapor phase). – Interphase momentum transfer includes drag, lift, lubrication, virtual mass and turbulent dispersion force. – Interphase mass transfer depends on interfacial heat transfer. – Assuming constant bubble number density for nucleation process.	– Flashing flow in case of transient pressure release in vertical pipe of Ref. [38]. – Choosing bubble diameter for model or bubble number density without experimental evaluation can lead to large deviation. – To improve accuracy of model, poly-disperse simulation using IMUSIG to consider bubble size change caused by phase change is performed instead of mono-disperse method.
[39] FLUENT 12.0	– Mixture model considering slip phenomenon between two phases. – Latent heat transfer considers affection of phase change phenomenon driven by pressure [40] and temperature. – Rate of phase change is based on sonic velocity equation [41] limiting in cases of homogeneous equilibrium and homogeneous frozen.	– Convergent-divergent motive nozzle of Ref. [42] inside a two-phase ejector is used for validation. – Results show an agreement between numerical method and experiment in term of pressure profile along divergent section.
[43] CFX 14.5	– Same model as in Ref. [37].	– Flashing of initial subcooled water flow in vertical convergent-divergent nozzle from Ref. [8]. – Calculated mass flow rate is acceptable in deviations to experiment (maximum relative error −6.8%). – Satisfy cross section averaged pressure and vapor fraction. However, radial distribution of vapor fraction is too uniform and have large deviations near nozzle outlet. – Choosing coefficients for flashing model as bubble number density and heat transfer coefficient need to be more information of experiment.
[44] CFX	– Same model as in Ref. [37] with different models for bubble number density (mono-disperse assumption and poly-disperse method).	– An overview of previous works with assumptions of both mono-disperse approach and poly-disperse approach. – For mono-disperse approach, assumptions can apply in case of nearly constant bubble size in flashing flow. – Poly-disperse approach is more interesting than monodisperse with open parameters, which can help to capture the change of the bubble size distributions. However, this method also needs more experimental information than monodisperse approach.
[45] In-house code	– A compressible homogeneous mixture approach. – Mass transfer models including: (i) pressure phase change model from Ref. [46] and (ii) thermal phase change model. – Empirical coefficients of phase change model are confirmed by modeling cavitating flow on a cylindrical head form and a Clark-Y hydrofoil geometry.	– Convergent-divergent nozzle geometry with operating conditions in Abuaf et al. [8] is used as experimental benchmark. Numerical results show a good agreement compared to measured data (maximum error in term of mass flow rate is 4.19%).

and proposes an improved model for flashing boiling flows, which includes the boiling delay effect. In the proposed model, based on the mixture two-phase approach, the phase change process depends on the difference between the vaporization pressure and the vapor partial pressure. The thermal nonequilibrium effects have been included by using ad hoc modeling of the boiling delay. The proposed model assumes constant bubble size distribution and it is based on a mixture model with slip velocity.

The paper is structured as follows: In Sec. 2, the physical phenomenon of flashing flow is presented and described. In Sec. 3, the experimental benchmark, including geometry of circular convergent-divergent nozzle and operating conditions, is discussed. In Sec. 4, the physical model and the numerical modeling approach are presented, including turbulence and phase-change modeling approaches. In Secs. 5 and 6, sensitivity analyses (turbulence models and model parameters) and validation of the numerical results are presented. Finally, the main conclusions and outcomes of the study are discussed in Sec. 7.

2 The Flashing Phenomenon

This section aims to provide an insight to the physical phenomena modeled, for the sake of completeness. To this end, Fig. 1(*a*) displays the thermodynamic diagram of water phase change in the boiling process. This process occurs at constant pressure in a saturation region under thermal equilibrium conditions (see Ref. [53] for further details). However, in practice (viz. high-speed flows, as ejector-based systems), the phase change inside nozzles is strongly related to nonequilibrium effects; for this reason, this diagram cannot be used to predict the fluid dynamics in the phase change region. In particular, when subcooled water flow enters the nozzle, the sudden depressurization leads to superheated water and, consequently, phase change occurs. In this case, the bubble nucleation process is related to the nonequilibrium effects [5]. Generally, the phase change process driven by an abrupt pressure drop is separated in three stages as displayed in Fig. 1(*b*) and summarized in the following:

(1) *Stage* 1. After the pressure drops below saturation pressure, the small nuclei existing in nonwettable rough wall cavities and in the bulk flow start growing. The behavior of the dispersed phase (viz. the bubbles) at this stage is dominated by the surface tension forces, which limit the growth of the nuclei (please notice that for this reason, this stage is called delay period in Ref. [54] or idle period in Ref. [55]). This boiling delay effect, which accounts for thermal nonequilibrium, has an influence on the global fluid dynamic quantities (i.e., the mass flow rate and the outlet vapor fraction).

(2) *Stage* 2. This stage starts when the diameter of the bubbles exceeds a critical radius (see Ref. [5]). The bubble development at this stage is dominated by the pressure difference between the bubble surface (viz. the dispersed phase) and the surrounding water (viz. the continuous phase). The bubble growth rate in this stage can be approximated by the Rayleigh–Plesset equation as in Ref. [56].

(3) *Stage* 3. This stage is dominated by heat transfer around the bubble interface. In this stage, a significant influence to heat transfer mechanism at water–bubble interface comes from turbulence fluctuations and relative motion between bubbles (viz. the dispersed phase) and the surrounding water (viz. the continuous phase) [57].

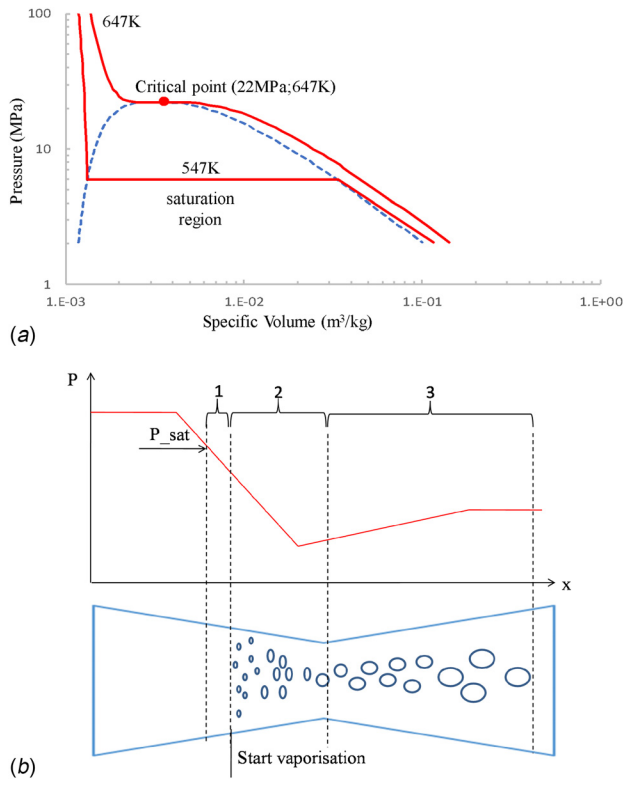

Fig. 1 Physical behavior of flashing flow: (*a*) thermodynamic diagram of phase change of water with equilibrium assumption and (*b*) start of vaporization

3 Experimental Benchmark

To validate the numerical results, the experimental measurements proposed by Abuaf [8] have been used. Abuaf has designed an experimental setup to measure net vapor generation rates with nonequilibrium conditions. In particular, this benchmark consists in a circular convergent-divergent nozzle, with subcooled water at the nozzle inlet and flashing flow at the outlet (please refer to Fig. 2 for the detailed dimensions of the nozzle). In the converging-diverging nozzle, 49 pressure taps and two windows for observation at the exit point have been used to measure (a) the pressure distributions, (b) the average vapor fraction along the axial direction of the nozzle, (c) the flashing inception point, and (d) and local radial void fraction profiles (viz., the vapor profiles) at different axial positions. The operating conditions of the experiments (i.e., pressure, temperature, and mass flow rates) are listed in Table 3. The interested reader may refer to Ref. [8] for more information about the experimental conditions.

4 Physical Model

4.1 Balance Equations and Physical Modeling. In this work, the axisymmetric two-phase mixture model, based on Ref. [47], has been applied to model the fluid dynamics of the convergent-divergent nozzle. Please note that in the following, all vectors are reported using the axial, x, and the radial, r, components; conversely, the slip velocity is used to couple the two phases (liquid and vapor).

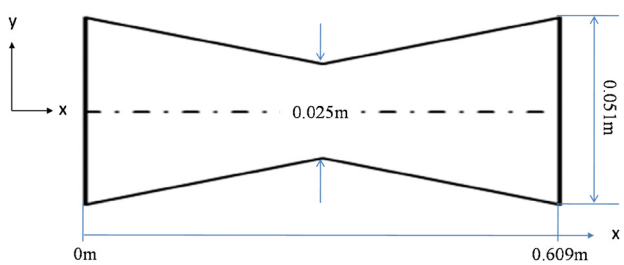

Fig. 2 Vertical circular convergent-divergent nozzle in Abuaf [8]

Table 3 Operating conditions and case code names in Ref. [8]

Case code name	Upstream pressure (Pa)	Inlet temperature (K)	Outlet pressure (Pa)	Flashing inception pressure (Pa)	Saturation pressure (Pa)	Mass flow rate (kg/s)
BNL284	530,000	422.35	456,000	404,700	466,000	7.3
BNL309	555,900	422.25	402,500	393,500	464,800	8.8
BNL273	573,500	421.85	442,100	419,200	459,800	8.7
BNL268	575,200	422.05	443,000	405,700	462,300	8.7
BNL304	577,700	422.15	441,000	399,700	463,500	8.8
BNL278	688,600	421.95	434,100	425,700	461,000	11.7
BNL296	764,900	421.95	432,600	417,000	461,000	13.1

The mass, the momentum, and the energy governing equations are formulated as follows:

4.1.1 *Mass Conservation*

$$\frac{\partial \rho_m}{\partial t} + \frac{\partial}{\partial x}(\rho_m v_{x,m}) + \frac{\partial}{\partial r}(\rho_m v_{r,m}) + \rho_m \frac{v_{r,m}}{r} = 0 \tag{1}$$

4.1.2 *Axial Momentum Conservation Equation*

$$\begin{aligned}
&\frac{\partial(\rho_m v_{x,m})}{\partial t} + \frac{1}{r}\frac{\partial}{\partial x}(r\rho_m v_{x,m} v_{x,m}) + \frac{1}{r}\frac{\partial}{\partial r}(r\rho_m v_{r,m} v_{x,m}) \\
&= -\frac{\partial p}{\partial \mathrm{x}} + \frac{1}{r}\frac{\partial}{\partial x}\left[r\mu_m\left(2\frac{\partial v_{x,m}}{\partial x} - \frac{2}{3}(\nabla \cdot \mathbf{v}_m)\right)\right] \\
&\quad + \frac{1}{r}\frac{\partial}{\partial r}\left[r\mu_m\left(\frac{\partial v_{x,m}}{\partial r} + \frac{\partial v_{r,m}}{\partial x}\right)\right] \\
&\quad + \sum_{k=1}^{n}\left[\frac{1}{r}\frac{\partial}{\partial x}(r\alpha_k\rho_k v_{dr_x,k} v_{dr_x,k}) + \frac{1}{r}\frac{\partial}{\partial r}(r\alpha_k\rho_k v_{dr_r,k} v_{dr_x,k})\right]
\end{aligned} \tag{2}$$

4.1.3 *Radial Momentum Conservation Equation*

$$\begin{aligned}
&\frac{\partial(\rho_m v_{r,m})}{\partial t} + \frac{1}{r}\frac{\partial}{\partial x}(r\rho_m v_{x,m} v_{r,m}) + \frac{1}{r}\frac{\partial}{\partial r}(r\rho_m v_{r,m} v_{r,m}) \\
&= -\frac{\partial p}{\partial \mathrm{r}} + \frac{1}{r}\frac{\partial}{\partial x}\left[r\mu_m\left(\frac{\partial v_{r,m}}{\partial x} + \frac{\partial v_{x,m}}{\partial r}\right)\right] \\
&\quad + \frac{1}{r}\frac{\partial}{\partial r}\left[r\mu_m\left(2\frac{\partial v_{r,m}}{\partial r} - \frac{2}{3}(\nabla \cdot \mathbf{v}_m)\right)\right] - 2\mu_m\frac{v_{r,m}}{r^2} \\
&\quad + \frac{2}{3}\frac{\mu_m}{r}(\nabla \cdot \mathbf{v}_m) \\
&\quad + \sum_{k=1}^{n}\left[\frac{1}{r}\frac{\partial}{\partial x}(r\alpha_k\rho_k v_{dr_x,k} v_{dr_r,k}) + \frac{1}{r}\frac{\partial}{\partial r}(r\alpha_k\rho_k v_{dr_r,k} v_{dr_r,k})\right]
\end{aligned} \tag{3}$$

where

$$\nabla \cdot \mathbf{v}_m = \frac{\partial v_{x,m}}{\partial x} + \frac{\partial v_{r,m}}{\partial r} + \frac{v_{r,m}}{r} \tag{4}$$

4.1.4 *Energy Conservation*

$$\begin{aligned}
&\frac{\partial\left(\sum_{k=1}^{n}\alpha_k\rho_k E_k\right)}{\partial t} + \sum_{k=1}^{n}\left[\alpha_k(\rho_k E_k + p)\left(\frac{\partial}{\partial x}(\rho_k v_{x,k}) + \frac{\partial}{\partial r}(\rho_k v_{r,k})\right.\right. \\
&\left.\left. + \rho_k\frac{v_{r,k}}{r}\right)\right] = \nabla \cdot (\lambda_{\mathrm{eff}}\nabla T)
\end{aligned} \tag{5}$$

In the governing equations Eqs. (1)–(5), the averaged-mass mixture velocity $\mathbf{v}_m$, the mixture density ρ_m, the mixture dynamic viscosity μ_m, and the effective conductivity λ_{eff} are defined as follows:

$$\mathbf{v}_m = \frac{\sum_{k=1}^{n}\alpha_k\rho_k\mathbf{v}_k}{\rho_m} \tag{6}$$

$$\rho_m = \sum_{k=1}^{n}\alpha_k\rho_k \tag{7}$$

$$\mu_m = \sum_{k=1}^{n}\alpha_k\mu_k \tag{8}$$

$$\lambda_{\mathrm{eff}} = \sum_{k=1}^{n}\alpha_k(\lambda_k + \lambda_t) \tag{9}$$

Please note that the energy equation of the mixture model used in this work neglects work contribution due to shear stresses. This assumption is applied in state-of-the-art mixture model, e.g., refers to Refs. [24], [37], [43], and [44], and is also implemented in the commercial code ANSYS-FLUENT 16.2 [58].

4.2 Slip Model. In the proposed approach, the slip model is formulated in term of the drift velocity, $\mathbf{v}_{dr,p}$. The drift velocity is defined as relative velocity between secondary phase velocity, $\mathbf{v}_p$, and mixture velocity, $\mathbf{v}_m$ [47]:

$$\mathbf{v}_{dr,p} = \mathbf{v}_p - \mathbf{v}_m \tag{10}$$

The relative velocity between primary phase (q) and secondary phase (p), $\mathbf{v}_{pq} = \mathbf{v}_p - \mathbf{v}_q$, is used to derive Eq. (11) from Eq. (10):

$$\mathbf{v}_{dr,p} = \mathbf{v}_{pq} - \sum_{k=1}^{n} c_k\mathbf{v}_{kq} \tag{11}$$

Please note that $c_k = \alpha_k\rho_k/\rho_m$ represents the mass fraction of phase kth.

Please note that the native formulation used in ANSYS-FLUENT to define $\mathbf{v}_{pq}$ is a modified version of Ref. [47], including a diffusion term for modeling the turbulence dispersion of dispersed phase

$$\mathbf{v}_{pq} = \frac{\tau_p}{f_{\mathrm{drag}}}\frac{(\rho_p - \rho_m)}{\rho_p}\mathbf{a} - \frac{\nu_m}{\alpha_p\sigma_D}\nabla\alpha_q \tag{12}$$

where ν_m and σ_D are the mixture turbulent viscosity and the Prandtl dispersion coefficients, respectively. Particle relaxation time of secondary phase τ_p is defined as follows:

$$\tau_p = \frac{\rho_p d_p^2}{18\mu_q} \tag{13}$$

where ρ_p and d_p are density and bubble diameter of secondary phase, respectively. μ_q is defined as dynamic viscosity of primary phase.

In Eq. (12), f_{drag} is the drag function, which is determined as in Ref. [59]

$$f_{\text{drag}} = \begin{cases} 1 + 0.15\text{Re}^{0.687} & \text{Re} \le 1000 \\ 0.0183\text{Re} & \text{Re} > 1000 \end{cases} \tag{14}$$

where Re is the relative Reynolds number function of the particle diameter d_p

$$\text{Re} = \frac{\rho_q |\mathbf{v}_p - \mathbf{v}_q| d_p}{\mu_q} \tag{15}$$

It should be noted that the mixture model in the commercial code ANSYS-FLUENT 16.2 only considers the slip effect between two phases, neglecting other nondrag forces, unlike the Euler multifluid one, which takes into account nondrag forces as well.

4.3 Phase Change Model. In this study, the phase change (vaporization phenomenon) is deemed driven by the pressure difference (please refer to Sec. 2), taking into account the thermal nonequilibrium effects by means of "artificial coefficients," as defined in the rest of this section.

The first step is to define the vapor transport equation, to be solved along with the other governing equations

$$\frac{\partial(\alpha_v \rho_v)}{\partial t} + \frac{\partial}{\partial x}(\alpha_v \rho_v v_{x,m}) + \frac{\partial}{\partial r}(\alpha_v \rho_v v_{r,m}) + \alpha_v \rho_v \frac{v_{r,m}}{r} = -\left[\frac{\partial}{\partial x}(\alpha_v \rho_v v_{dr_x}) + \frac{\partial}{\partial r}(\alpha_v \rho_v v_{dr_r}) + \alpha_v \rho_v \frac{v_{dr_r}}{r}\right] + \dot{m} \tag{16}$$

In this work, the mass source term is a modified version of the Lee model [60], considering Clapeyron–Clausius equation to transform thermal phase change model to phase change model driven by pressure.

The change of phase source terms of the Lee model [60] reads as follows:

$$\dot{m} = A_i F = A_i \beta \sqrt{\frac{M}{2\pi R T_{\text{sat}}}} L \left(\frac{\rho_v \rho_l}{\rho_l - \rho_v}\right) \frac{(T^* - T_{\text{sat}})}{T_{\text{sat}}} \tag{17}$$

where T^* is the vapor temperature at the interface and is assumed to be close to T_{sat}. L, and A_i are the latent heat and interfacial area density, respectively. β is an "accommodation" coefficient and must be chosen following different operating conditions (sensitivity analysis has been carried out in rest of this paper).

The relationship between pressure and temperature at the saturation condition is accounted by the Clapeyron–Clausius equation as in Eq. (18)

$$\frac{dP}{dT} = \frac{L}{T}\left(\frac{\rho_v \rho_l}{\rho_l - \rho_v}\right) \tag{18}$$

From Eq. (18), the variation of pressure near saturation conditions can be derived as in the following equation:

$$(P_{\text{sat}} - P^*) = \frac{L}{T}\left(\frac{\rho_v \rho_l}{\rho_l - \rho_v}\right)(T^* - T_{\text{sat}}) \tag{19}$$

where P^* is the partial pressure at interface on the vapor side with value close to saturation pressure, P_{sat}.

Finally, the mass source term for the vapor transport at the interface is defined as follows:

$$\dot{m} = A_i F = A_i \beta \sqrt{\frac{M}{2\pi R T_{\text{sat}}}} (P_{\text{sat}} - P^*) \tag{20}$$

In this study, the interfacial area density is modeled following the proposal of Liao and Lucas [43], as defined in Eq. (13)

$$A_i = (6\alpha_v)^{\frac{2}{3}} (\pi N_b)^{\frac{1}{3}} \tag{21}$$

N_b is bubble number density. In this work, distribution of bubble and phenomena of bubble dynamics such as bubble break-up and coalescence are neglected. For this reason, N_b is imposed a constant value for all tested cases.

It should be noted that Eq. (20) is applied in case of evaporation without turbulence effects. To account for the local turbulence effects in flashing flows, the formula of the vaporization pressure, as defined in Ref. [61], is applied. This formulation reads

$$P_v = P_{\text{sat}} + 0.195\rho k \tag{22}$$

Finally, the source term for the mass flux at the interface is accounted as follows:

$$\dot{m} = A_i F = A_i \beta \sqrt{\frac{M}{2\pi R T_{\text{sat}}}} (P_v - P^*) \tag{23}$$

Taking into account Eqs. (22) and (23), Eq. (24) can be also written

$$\dot{m} = A_i F = A_i \beta \sqrt{\frac{M}{2\pi R T_{\text{sat}}}} (0.195\rho k + P_{\text{sat}} - P^*) \tag{24}$$

In this model, the value of $dp = P_{\text{sat}} - P^*$ should be small enough; please refer to the sensitivity analysis section of artificial coefficients to have a guideline for the value of dp.

From a practical point of view, it should be noted that the evaporation model in the present work does not use default evaporation solver of ANSYS-FLUENT 16.2. In this work, a user-defined function is developed to insert into the source term of vapor fraction transport for flexibility. The user-defined function has been implemented following the procedure set out in Ref. [62] to verify the correct implementation and avoid possible user errors.

4.4 Turbulence Modeling. The turbulent behavior has been treated using the RANS approach. In particular, six RANS turbulence models have been tested and compared: standard $k-\varepsilon$, realizable $k-\varepsilon$, RNG $k-\varepsilon$, standard $k-\omega$, $k-\omega$ stress shear transport (SST), and root-mean-square (RMS). These models are well known in the literature and have a wide application range in industry. For further information about their mathematical formulation, the reader should refer to the original references set out in Table 4. In addition, the reader should refer to Ref. [58] for further information about their implementation in the commercial code ANSYS-FLUENT 16.2. All the examined models have been used in their original implementation without further modifications. Besides turbulence models, the near-wall formulation should be considered. Standard $k-\omega$, $k-\omega$ SST models do not need a near-wall treatment because their mathematical structure already emphasizes the flow close to the wall. However, some aspects, in their ANSYS-FLUENT 16.2 implementations, have to be considered. Concerning the standard $k-\omega$ and the $k-\omega$ SST, a low-

Table 4 References of turbulence models

Turbulence models	References
Standard $k-\epsilon$	[63]
Realizable $k-\epsilon$	[64]
RNG $k-\epsilon$	[65]
RSM	[66]
Standard $k-\omega$	[67–70]
$k-\omega$ SST	[71–74]

Table 5 References of wall treatments for turbulence models

Wall treatment	Standard $k-\epsilon$	Realizable $k-\epsilon$	RNG $k-\epsilon$	RSM
Standard wall function		[75]		
Nonequilibrium wall function		[76]		
Scalable wall function		User's guide of ANSYS FLUENT rel. 16.2 [58]		
Enhanced wall treatment		User's guide of ANSYS FLUENT rel. 16.2 [58]		
	Standard $k-\omega$	$k-\omega$ SST		
Standard	User's guide of ANSYS FLUENT rel. 16.2 [58]			
Low-re corrections	User's guide of ANSYS FLUENT rel. 16.2 [58]			

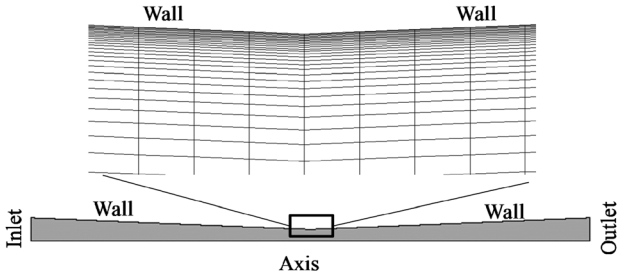

Fig. 3 Mesh and boundary condition of convergent-divergent nozzle

Table 6 Boundary conditions

Boundary	Flow boundary	Turbulence boundary
Inlet	Total pressure	Turbulence intensity and hydraulic diameter
Outlet	Static pressure	
Wall	Adiabatic wall	Wall function
Axis	Axisymmetric	Axisymmetric

Reynolds implementation may be enabled in ANSYS-FLUENT 16.2 to fully resolve near-wall grids. Conversely, the standard $k-\varepsilon$, realizable $k-\varepsilon$, RNG $k-\varepsilon$, and RMS models require a near-wall modeling. In the present study, a sensitivity analysis on the following wall treatments has been performed, consistently with previous studies proposed by some of the authors (see Refs. [77] and [78]). The reader should refer to the references reported in Table 5 for further information concerning the near-wall treatments.

4.5 Numerical Domain and Boundary Conditions. The computational domain has been set up with structured quadrilateral elements (maximum skewness below 0.05, minimum orthogonal quality higher than 0.95) and two-dimensional axisymmetric approach. Figure 3 and Table 6 present mesh and boundary conditions applied in the simulations. In the benchmark cases, reversed flow did not occur at the outlet and this is the reason why only outlet static pressure is imposed to generate the pressure drop inside the nozzle. Please note that a grid independency study has been performed and is presented in Sec. 5.1. In addition, note that sensitivity analysis for the turbulence models and boundary conditions are presented in the discussion of the results (Secs. 5.2 and 5.3). As a result of the analysis concerning the influence of the use of different turbulence models along with the flashing model, the $k-\omega$ SST with standard option for the near-wall treatment was chosen to be used for the following analyses.

4.6 Numerical Setup. The proposed approach employs pressure-implicit with splitting of operators scheme for pressure–velocity coupling algorithm and second-order implicit scheme for the transient term, while information for the spatial discretization of different quantities is shown in Table 7. Due to the transient formulation, the time-step is fixed to 10^{-5} s with convergence criteria including (i) mass balance between inlet and outlet (<2% of relative error) and (ii) the maximum residual of all equations below 10^{-6}. Artificial coefficients, including bubble number density and maximum of difference between P^* and $P_{sat}(dp = P_{sat} - P^*)$, are set at the values of 4×10^8 and 75 Pa, respectively. It should be noticed that $dp = 75$ Pa is selected after performing sensitivity analysis with all operating conditions in this paper. The accommodation coefficient applied for boiling delay effect has been defined in range from 0.8 to 1.2 for each test case. It is worth noting that, in order to trig the phase change process, a vapor fraction of 10^{-5} has been imposed at the inlet. It is worth noting that, to evaluate the particle relaxation time, τ_p, and the relative Reynolds number, Re, the bubble diameter of the secondary phase, d_p, has been set equal to 10^{-5} m; it is important to observe that the present equivalent diameter is in asymptotic range of the drag coefficient.

Table 7 Numerical method

Discretization	Scheme
Transient formulation	Second-order implicit
Pressure–velocity coupling	Pressure-implicit with splitting of operators
Gradient	Green-gauss cell based
Pressure	PRESTO! [58]
Density	Second-order upwind
Momentum	
Volume fraction	
Turbulence kinetic energy	
Specific dissipation rate	
Energy	

5 Sensitivity Analysis

In this section, different sensitivity analyses concerning (a) grid convergence index (GCI), (b) turbulence models (RANS), (c) near-wall treatments, (d) turbulence inlet parameters, and (e) semi-empirical coefficients have been performed.

5.1 Grid Convergence Index. In order to assess the grid independency, a GCI analysis [79] has been applied to the case BNL309 using four different meshes consisting of: (a) 21,350, (b) 53,184, (c) 109,728, and (d) 214,650 elements, with an element ratio for all meshes $N_{i+1}/N_i \approx 2$ and the value of y^+ ranging from 6 to 16 for all tested meshes. Operating conditions used for the GCI analysis refer to the case of BNL309 using a k–ω SST model with standard option for the near-wall treatment for turbulence modeling (refer to Sec. 5.2 for turbulence model selection). The values of (a) the mass flow rate, (b) average vapor fraction at the outlet, and (c) average radial turbulence kinetic energy at throat level for the analyzed meshes are presented in Table 8, showing a

Table 8 Mesh independency study: grid convergence index

Mesh elements	Mass flow rate (kg/s)	Average vapor fraction at outlet	Average radial turbulence kinetic energy at throat (m^2/s^2)
21,350	8.63	0.765132	0.138114
53,184	8.79	0.762243	0.125219
109,728	8.82	0.762015	0.123920
214,650	8.82	0.762013	0.123901

Grid convergence index

Constant grid refinement ratio (r)	2
The order of convergence (p)	2.415
Mass flow rate with zero grid spacing (f^*)	8.827
Asymptotic range of convergence (C)	1.0034

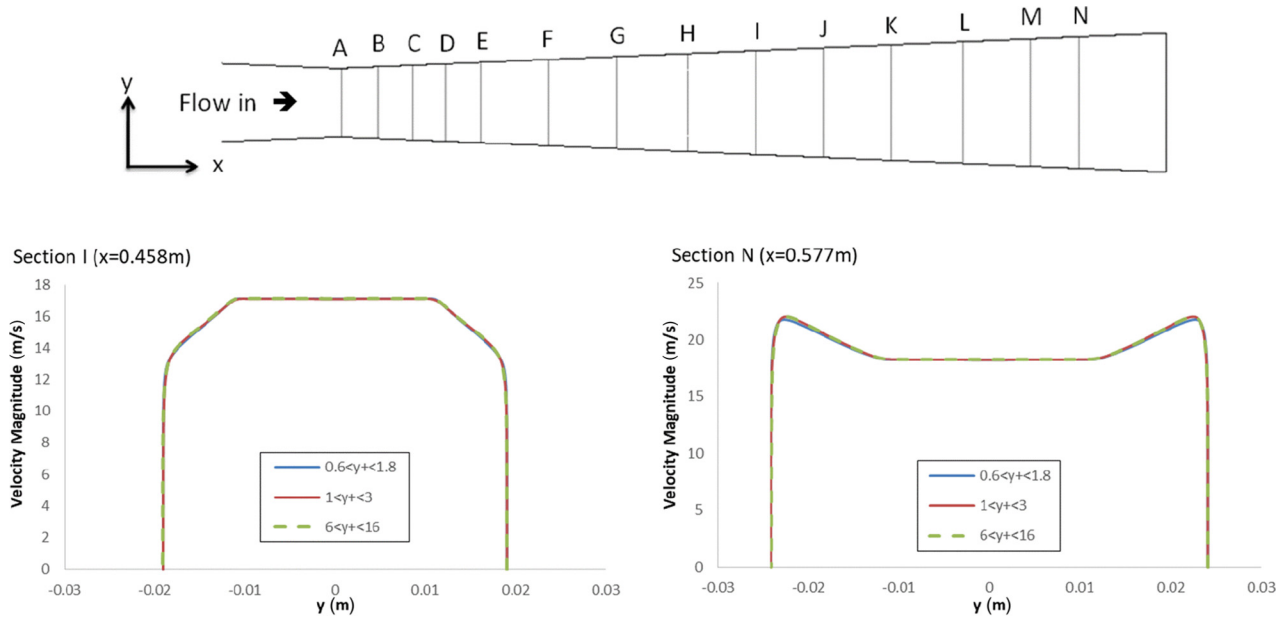

Fig. 4 Influence of y^+ on the velocity profile at cross section I ($x = 0.458$ m) and cross section N ($x = 0.577$ m)

Table 9 Mass flow rate relative error of BNL309 in analysis of turbulence models and wall treatments

Wall treatment	Standard k–ϵ	Realizable k–ϵ	RNG $k-\epsilon$	RSM
Standard wall function	−3.9%	+0.1%	−2.5%	−0.1%
nonequilibrium wall function	−5.9%	−2.1%	−4.7%	−1.2%
Scalable wall function	−3.7%	+0.1%	−2.3%	−0.2%
Enhanced wall treatment	−4.1%	−1.3%	−3.2%	−3.0%
k–ω options	Standard k–ω	k–ω SST		
Standard	+1.7%	+0.2%		
Low-re corrections	+4.0%	+2.0%		

very limited difference and coherent trend varying the number of elements. A more detailed GCI analysis applied to mass flow rate quantity for meshes (a) 21,350, (b) 53,184, and (c) 109,728 elements shows that an asymptotic behavior is reached (asymptotic range of convergence is 1.0034), with an error of 0.52% for grid (b) and 0.098% for grid (c) as regards the exact value of 8.82 kg/s. According to Table 8 values and GCI results, the mesh (c) (109,728 elements) has been selected for the analysis performed in this study.

The influence of the near-wall refinement is also evaluated in terms of y^+ parameter, observing a negligible influence on mass flow rate prediction. Furthermore, results obtained with different meshes ranging from $y^+ \approx 1$ to $y^+ < 16$ show a negligible deviation of velocity profile, as reported in Fig. 4.

5.2 Screening of Turbulence Models. The relative errors between experimental data and numerical results in terms of mass flow rate for case BNL309 are summarized in Table 9. As previously stated, in this study, six turbulence RANS models (standard k–ε, realizable k–ε, RNG k–ε, standard k–ω, k–ω SST, and RMS) with different near-wall treatments have been coupled with the

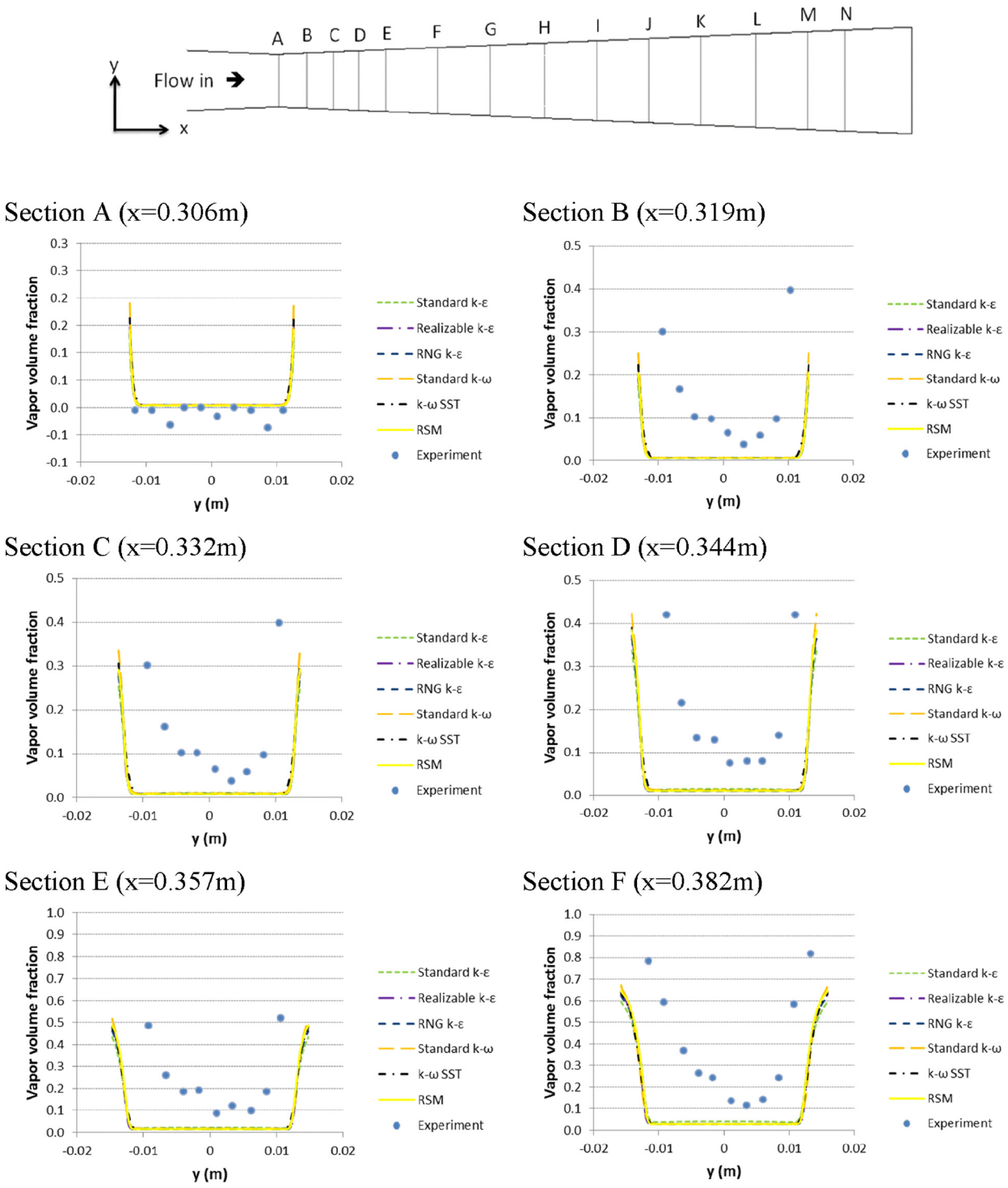

Fig. 5 Section description and radial vapor profile with effects of turbulence RANS models

flashing flow model to analysis the effects of turbulence model on phase-change process prediction.

All RANS models with different near-wall treatments have shown an acceptable relative error (below 6%). In particular, the standard $k-\varepsilon$ has resulted in larger errors, ranging from -3.9% to -5.9% (underestimation), compared to other RANS turbulence models. A better agreement with the experimental data has been achieved with the realizable k–ε and, with error ranging from $+0.1\%$ to -1.3% and from $+0.2\%$ to -2%, respectively. In addition, a local analysis of the effect of the turbulence RANS model to the radial profile of the vapor volume fraction is presented in Fig. 5. The Standard k–ε model overestimates vapor fraction at the center of the nozzle from position $x = 0.559$ m to the outlet of the convergent-divergent nozzle explaining the correspondingly lower mass flow rate, as illustrated in Table 10.

However, no significant differences of axial vapor profile for the different turbulence RANS models have been observed. Finally, k–ω SST with standard option for the near-wall treatment

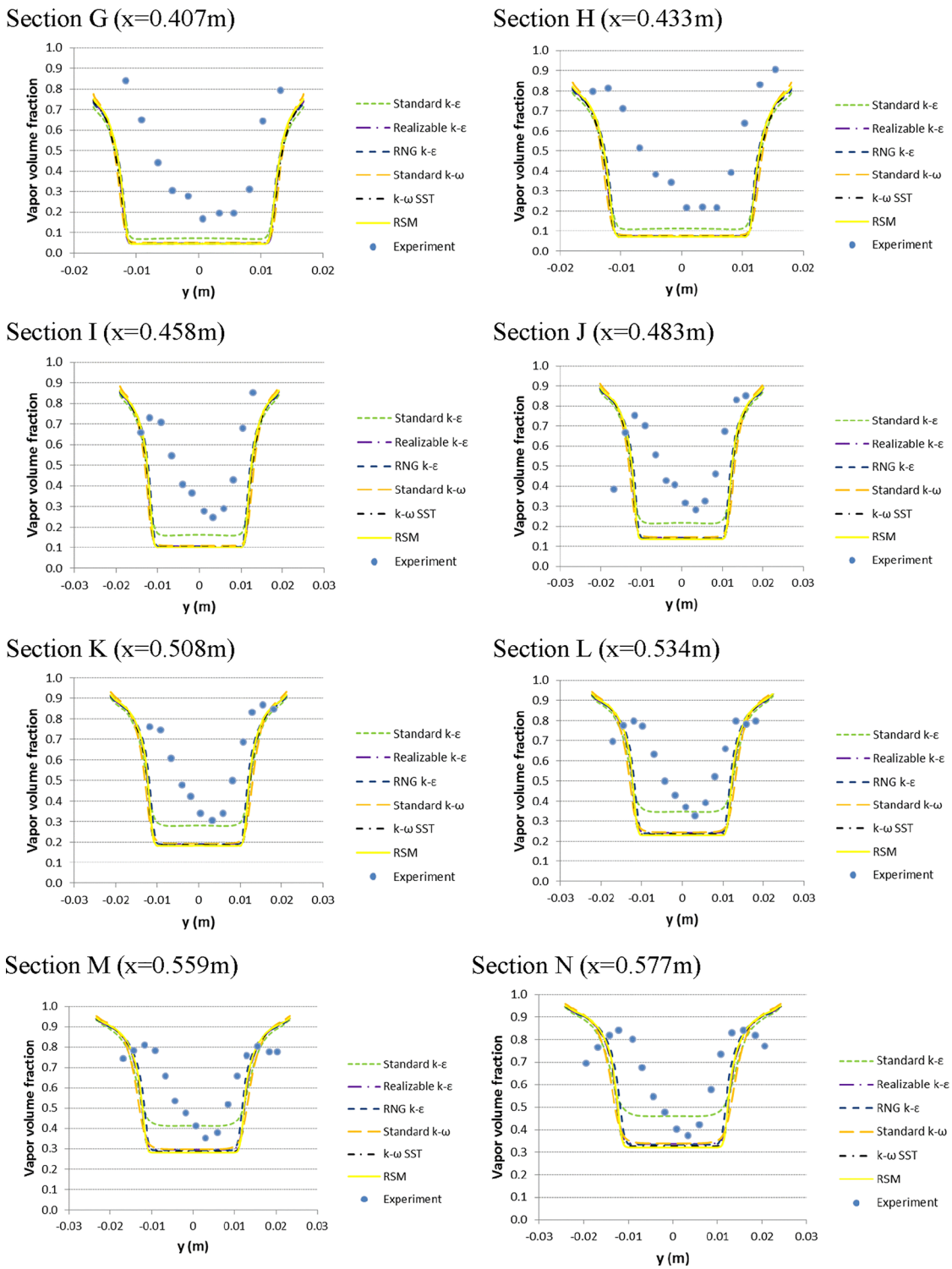

Fig. 5 (Continued)

Table 10 Sensitivity of turbulence inlet intensity to mass flow rate in case of BNL309

Turbulence inlet intensity	1%	2%	3%	4%	5%
Mass flow rate (kg/s)	8.82	8.78	8.76	8.70	8.64
Relative error compared to experimental data	0.2%	−0.2%	−0.4%	−1.1%	−1.8%

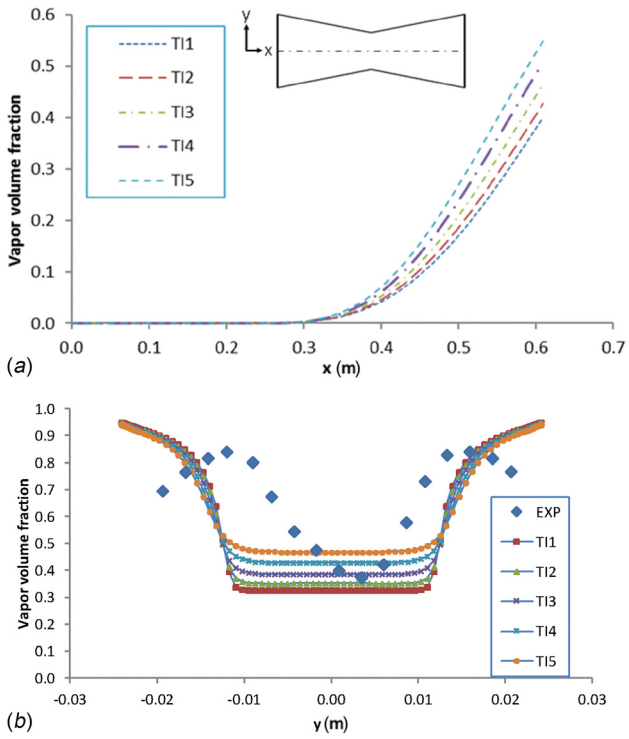

Fig. 6 Influence of turbulence inlet intensity to numerical results: (*a*) vapor fraction along center line and (*b*) radial vapor profile at $x = 0.577$ m

Table 11 Comparison of experimental mass flow rate and CFD mass flow rate

Cases	Accommodation coefficient β	Experimental mass flow rate (kg/s)	CFD mass flow rate (kg/s)	Relative error
BNL284	0.8	7.3	7.7	+5.4%
BNL309	1.2	8.8	8.8	+0.2%
BNL273	1.05	8.7	9.3	+6.8%
BNL268	1.0	8.7	9.2	+5.7%
BNL304	1.11	8.8	9.1	+3.4%
BNL278	1.15	11.7	12.3	+5.1%
BNL296	1.18	13.1	13.9	+6.1%

shows the best agreement with experimental data in both mass flow rate and trend of vapor profile along the nozzle. Thus, this model was used in the following analyzes.

5.3 Turbulence Inlet Intensity. Turbulence boundary conditions at the inlet of the nozzle have been defined by imposing: (a) hydraulic diameter and (b) turbulence intensity. The hydraulic diameter has been imposed equal to 0.051 m, which has been chosen according to the real geometry. Conversely, the turbulence intensity has been varied ranging from 1% to 5%. Figure 6 and Table 10 display the results concerning the influence of the inlet turbulent intensity on (a) the mass flow rate, (b) the average vapor fraction along the nozzle, and (c) the vapor fraction profile at $x = 0.577$ m. It is found that a turbulence inlet intensity of 1% shows the best accuracy, compared to the other turbulent intensity, in terms of both relative error of the global quantities (0.2%) and agreement of vapor fraction profile at $x = 0.577$ m. For this reason, a turbulence inlet intensity of 1% has been selected for the subsequent analysis.

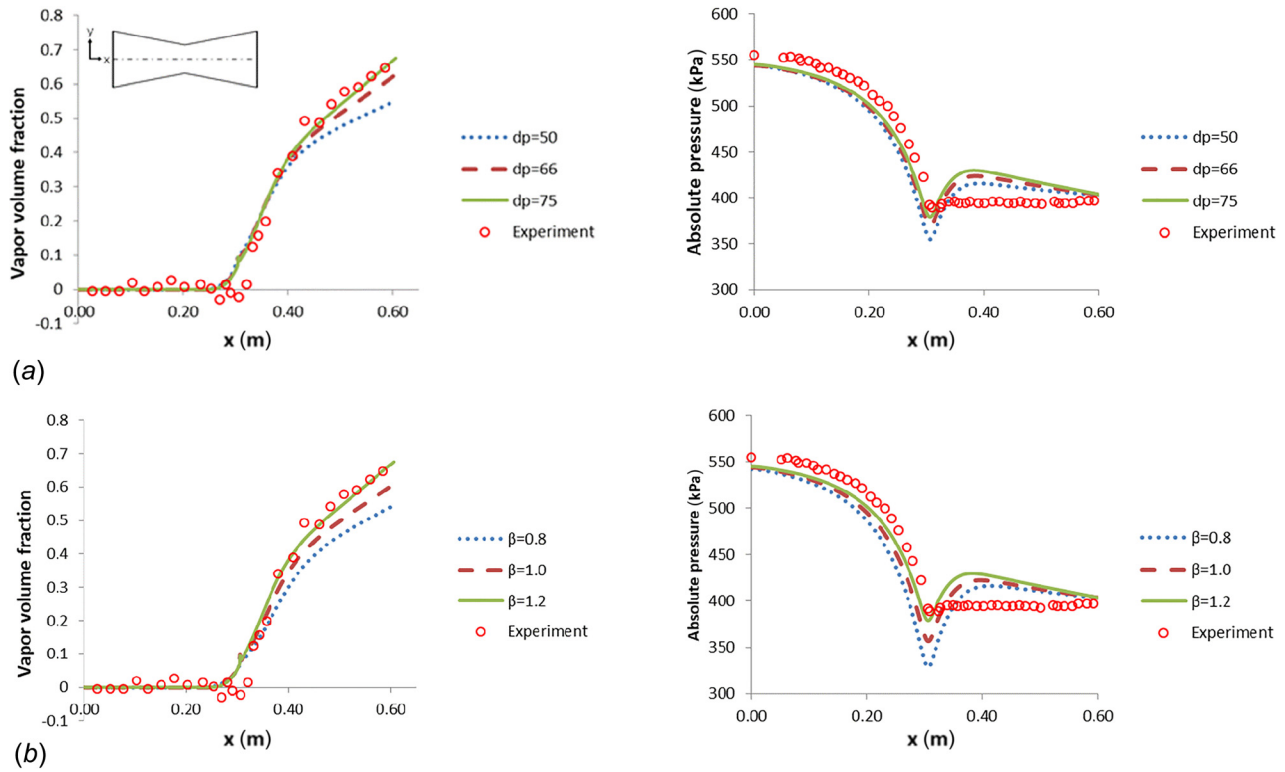

Fig. 7 Artificial coefficients sensitivity in BNL309: (*a*) vapor profile and static pressure along nozzle with fixed $d_p = 75$ Pa and (*b*) vapor profile and static pressure along nozzle with fixed $\beta = 1.2$

Table 12 Comparison of present model with Liao and Janet models for case BNL309

				Janet models [24]				
	Experiment	Present model	Liao model [43]	Blinkov model	Blinkov model with coal.	RPI model (default)	RPI model (fitted)	Riznic model (fitted)
Mass flow rate (kg/s)	8.8	8.8	8.4	8.39	8.27	10.20	8.10	9.15

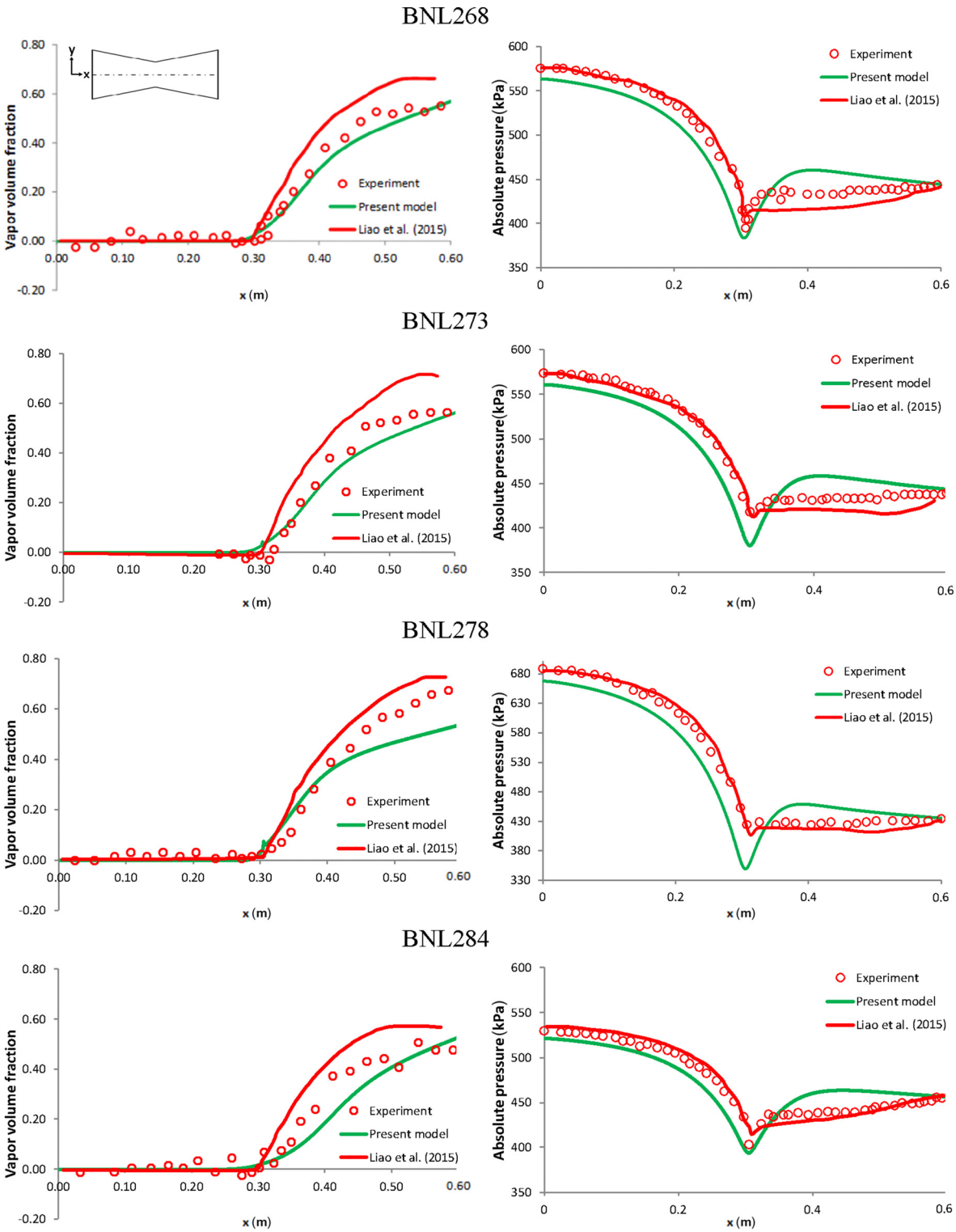

Fig. 8 Averaged vapor fraction and absolute pressure along nozzle compared to experimental data and Liao and Lucas model [43]

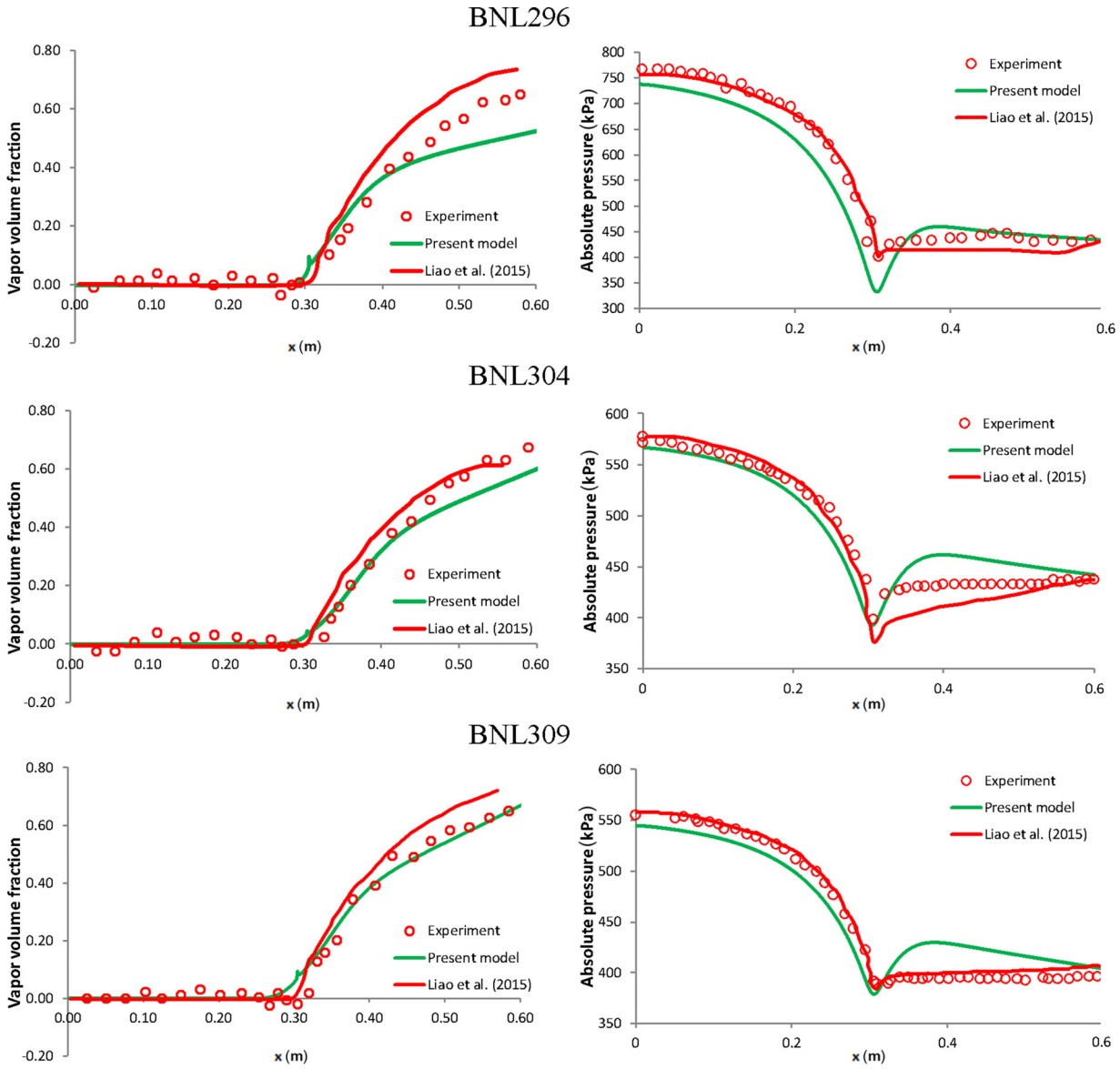

Fig. 8 (Continued)

It should be noted that the phase-change model is strongly influenced by turbulent kinetic energy. This leads to a stronger vaporization process (increase of vapor fraction at divergent parts of the nozzle and decrease of mass flow rate) corresponding to increase of the inlet turbulence intensity. Furthermore, CFD results are quite sensitive to the turbulence inlet boundary conditions and, from a theoretical point of view, an evaluation on uncertainty of the inlet turbulence should be performed.

5.4 Artificial Coefficients for Thermal Nonequilibrium Effect. The influence of artificial coefficients on flashing flow for case BNL309 was evaluated by changing different coefficients with a systematic procedure to evaluate their effect separately. First, dp is fixed to 75 Pa and a sensitivity analysis of the accommodation coefficient, β, is performed. Then, fixing $\beta = 1.2$, the same analysis is performed varying dp. In general, the increase of either β or dp leads to higher vapor volume fraction at divergent sections, as shown in Fig. 7. For static pressure along nozzle, the increase of artificial coefficients shows the increase of pressure at the throat region. This can be explained by earlier vaporization process. From convergent part to throat, water flow is incompressible, which gives us an explicit relation between static pressure and velocity. The increase of velocity leads to decrease of static pressure and vice versa. However, if vaporization happens earlier at throat level, the flow becomes compressible and static pressure in this region does not keep decreasing further with the increase of velocity.

6 Numerical Results

In this section, the results obtained with the present model are compared, in terms of both global and local fluid dynamic quantities, with available experimental data [8], as well as with numerical simulations by Liao and Lucas [43] and Janet et al. [24].

Unlike the present model, the modeling approach developed and applied by Wu et al. [31] and Liao et al. [43] requires the definition of the number of nuclei, by using available experimental data, to control the boiling delay effect. Janet et al. [24] used instead a more complex model, including bubble transport through source terms based on one-dimensional nucleation and coalescence modeling.

In the present study, the nucleation stage has been neglected, assuming a constant bubble number density $\left(N_b = 4 \times 10^8\right)$ and introducing an accommodation coefficient to control the boiling delay. In this section, a comparison between different results is reported, in

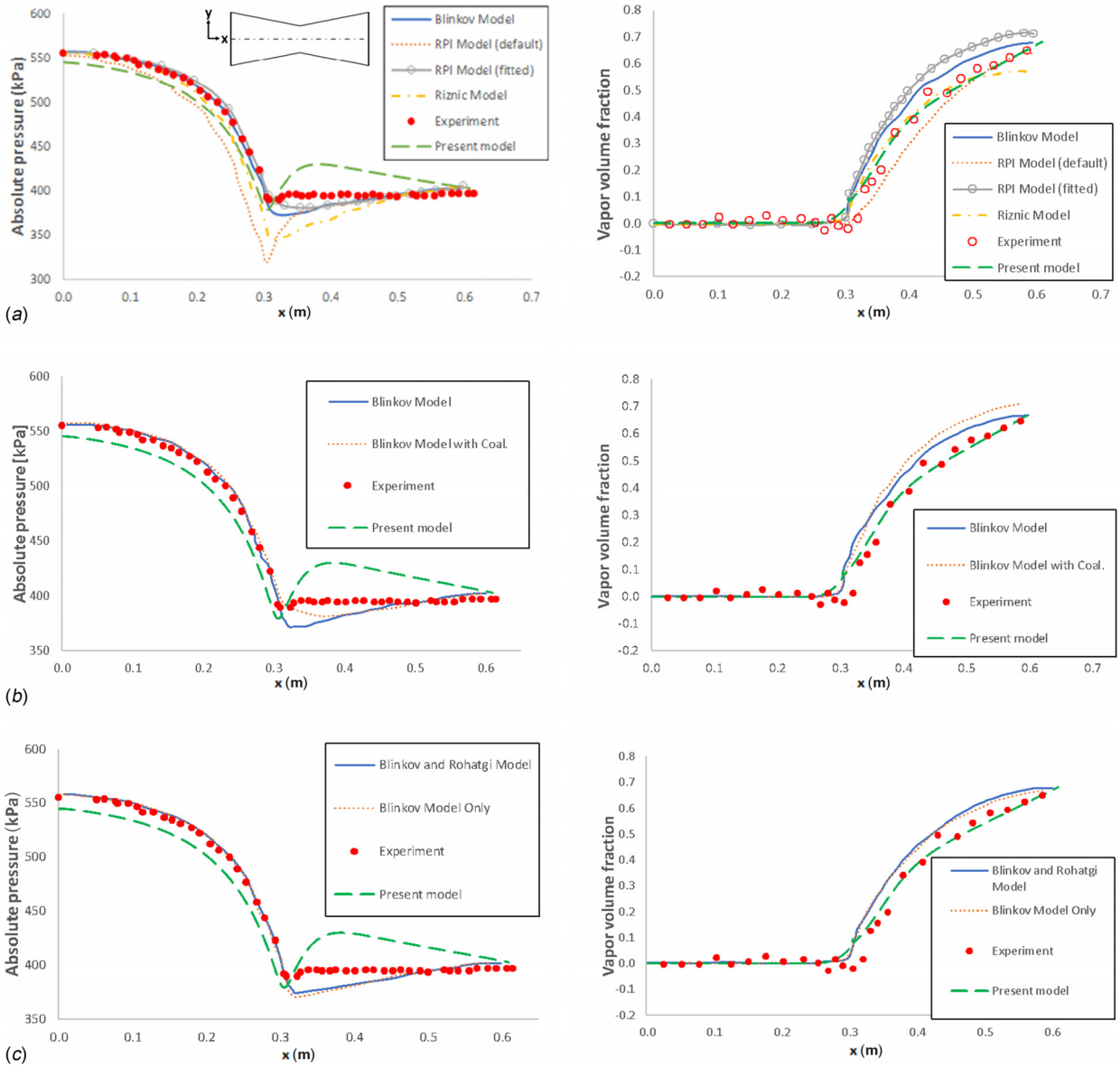

Fig. 9 Averaged vapor fraction and absolute pressure along nozzle compared to experimental data and Janet model [24]

terms of global (mass flow rate, vapor volume fraction, and pressure drop) and local (vapor volume fraction profile) quantities.

6.1 Global Results. Based on an experimental benchmark case, different operating conditions have been analyzed in this section comparing different global fluid dynamic quantities, such as mass flow rate, vapor volume fraction, and absolute pressure.

In Table 11, the computed mass flow rate has been compared to the experimental data for all the available operating conditions, showing average and maximum relative errors equal to 4.7% and 6.8%, respectively. According to Table 11, the accommodation coefficient was set to a value close to unity for all cases, obtaining a numerical mass flow rate slightly overestimating measured data for all cases. This can be related to the accuracy of the model predicting the pressure drop along the nozzle and the need for artificial coefficients to model the whole phenomenon, influencing the model capability to accurately reproduce the phenomenon. Furthermore, a comparison between the present model, Liao and Lucas [43], and Janet et al.'s [24] models is presented in Table 12 for case BNL309 in terms of mass flow rate. The present model shows a better prediction of experimental data, with a very limited difference on mass flow rate value, with other models showing errors ranging from 4% (Riznic fitted model) up to 16% (RPI default model).

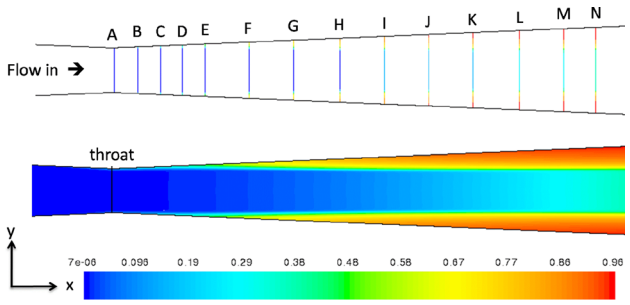

Fig. 10 Radial void fraction profile at positions along divergent nozzle

A more specific analysis has been carried out comparing average vapor fractions and absolute pressures along the nozzle shown in Fig. 8. The results for all the operating conditions show a general agreement of the present model with the experimental data. The numerical average vapor volume fraction at the convergent part is close to zero and starts increasing near the nozzle throat ($x = 0.3045$ m) up to the nozzle outlet, coherently with the behavior observed in the experimental data. Furthermore, in most of the operating conditions (BNL268, BNL273, BNL284, BNL304, and BNL309), the average vapor

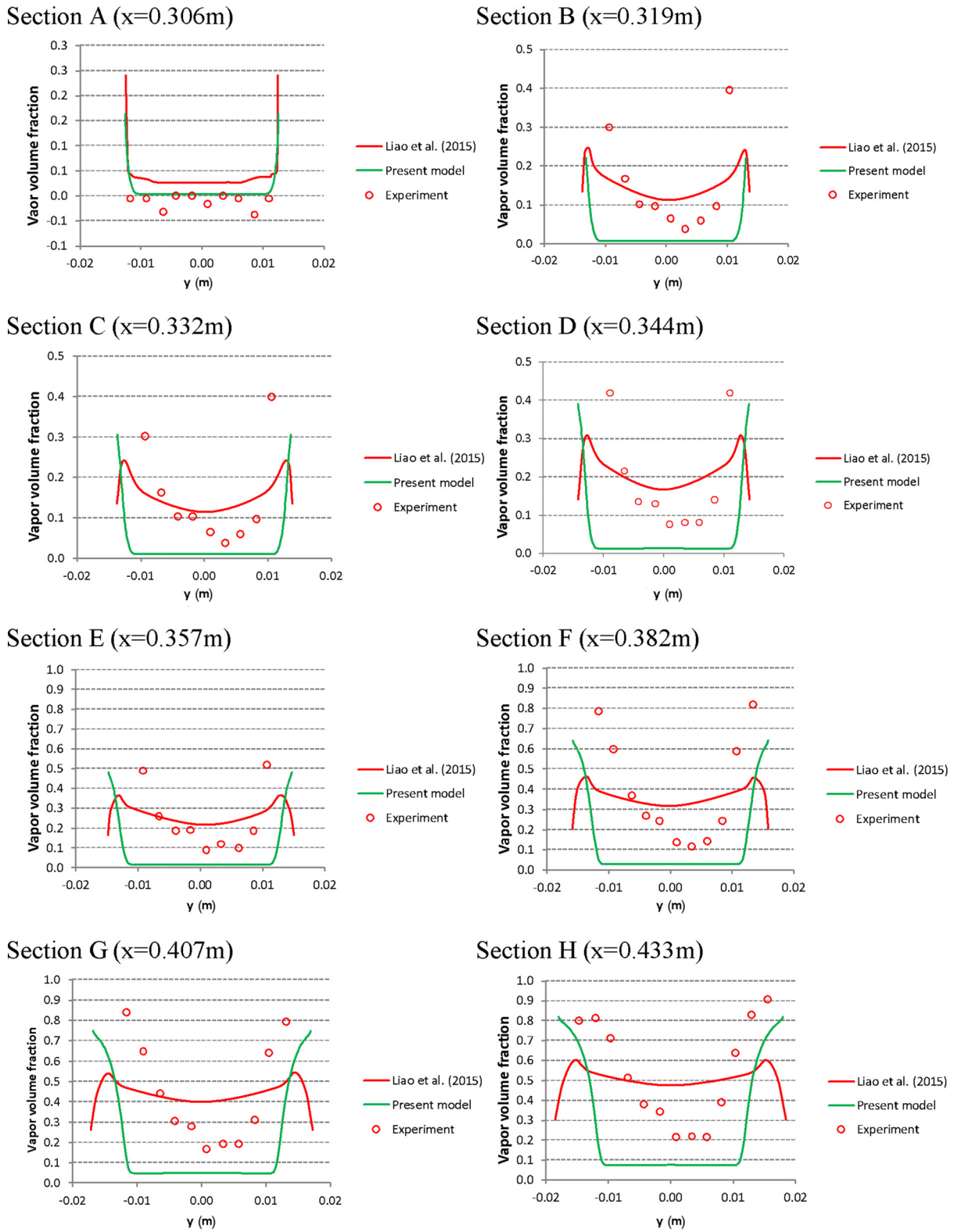

Fig. 11 Radial vapor profile of BNL309 compared to experiment data and Liao and Lucas model [43]

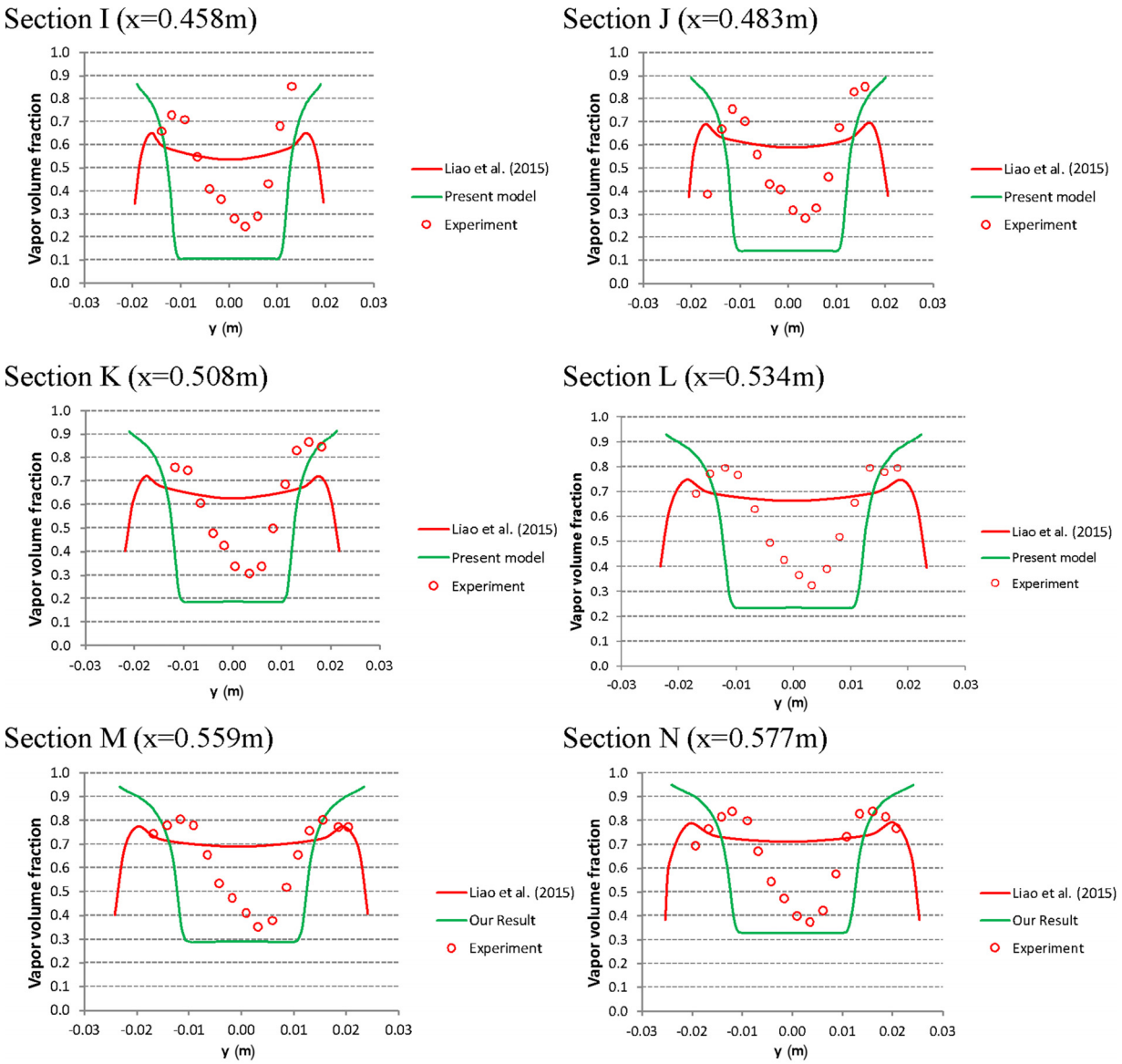

Fig. 11 (Continued)

volume fraction along the nozzle is well predicted by the present model, confirming its capability to correctly capture the flashing inception position.

For the absolute pressure at the convergent section of the nozzle, the depressurization trends are in line with measured data, whereas at the divergent section, a slight difference regarding the pressure wave type is observed. This is mainly due to neglecting the pressure jump across the interface and to the limits of the mixture model, only considering slip effects between two phases and neglecting other interfacial forces such as lift, drag, wall lubrication, and turbulent dispersion force. Furthermore, a slight difference on static pressure value at the inlet section is observed between numerical and experimental data, as reported in Figs. 8 and 9, where the maximum difference is below 5%. This can be related to the boundary condition used at the inlet, where total pressure is imposed and the static pressure value is influenced by the prediction of the dynamic contribution.

Further comparison with the numerical results of Ref. [24] has been performed. In their study, the effects of nucleation and

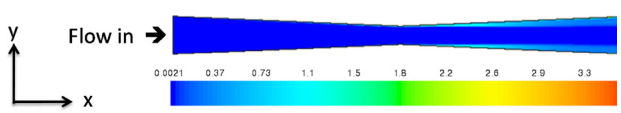

Fig. 12 Turbulence kinetic energy field

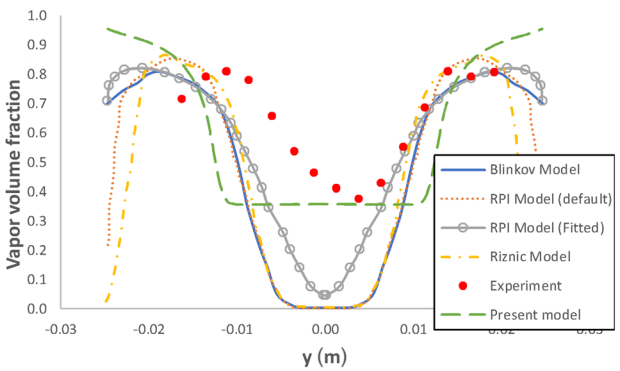

Fig. 13 Radial vapor fraction in comparison with results of Ref. [24] — $x = 0.59$ m

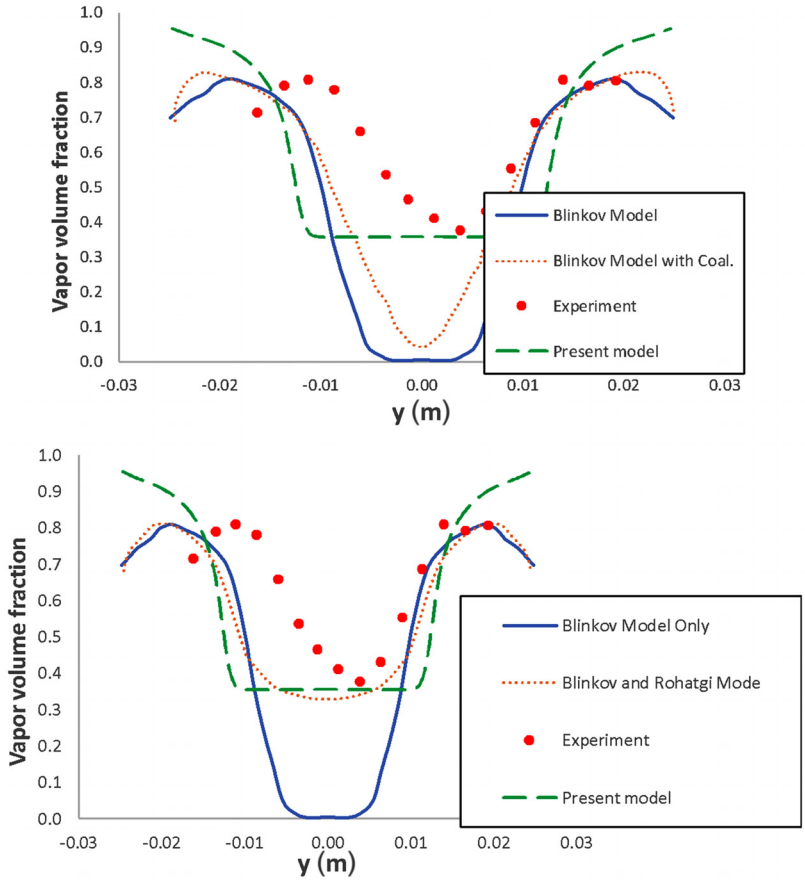

Fig. 14 Radial vapor fraction in comparison with results of Ref. [24]: (*a*) $x = 0.59$ m and (*b*) $x = 0.59$ m

coalescence are modeled by including a source term derived from one-dimensional physical modeling of the bubble transport equation. Janet and co-authors used different nucleation models, including Blinkov model [18], RPI model [25–27], RPI model with optimal parameters and Riznic model [28,29] for case BNL309. Absolute static pressure and average vapor fraction have been compared: vapor RPI model (default version) and Riznic models underpredict the static pressure near the nozzle throat, while all the models show a good accuracy reproducing the average vapor fraction value, as shown in Fig. 9(*a*). In Figs. 9(*b*) and 9(*c*), the static pressure and average vapor fraction are evaluated using the present model and the Blinkov model considering the coalescence effect, showing a good level of agreement with the experimental data.

For all the analyzed global fluid dynamic quantities, the proposed CFD flashing model shows a good prediction with respect to experimental data as well as to other models that include the nucleation process.

6.2 Local Results. Figures 10 and 11 provide an insight view of radial vapor distribution for case BNL309 with the starting position near the nozzle throat ($x = 0.306$ m) and the final position at $x = 0.577$ m near the nozzle outlet.

The present model has been compared with experimental data and Liao and Lucas [43] model at different sections across the nozzle. At $x = 0.306$ (position A), experimental data show a vapor volume fraction value equals to zero, whereas the present and Liao models show a peak near the wall region, implying an earlier flashing inception. From $x = 0.319$ m to $x = 0.577$ m (positions B, C, and D), a peak of vapor fraction near the wall has been observed in Ref. [43], which does not appear in the experimental data. Besides, in Liao et al., vapor fraction at the central region also develops faster than measured data. All the differences described above can be associated with the assumed bubble number density, leading to uncontrollable local behaviors of flashing flow (increasing vapor fraction near the wall is too low and in central region is too high), as better explained in Ref. [43].

The present model, based on a phase change model driven by pressure, is able to take into account the turbulence effects near the wall, showing a better agreement with the experimental data in sections from $x = 0.319$ m to $x = 0.577$ m (see Fig. 12). However, local predicted results still show some discrepancies compared to experiment. Indeed, neglecting bubble coalescence and migration causes the underprediction of the thickness of the vapor region near the wall. Additionally, bubble migration is observed from sections H to N in the experimental data, with the vapor fraction peak moving from the wall into the bulk region, whereas this behavior is not captured by the present model as shown in Fig. 11. Furthermore, results obtained with Ref. [24] models show a general underprediction of the experimental data, especially in the bulk region of the nozzle, as shown in Fig. 9 due to ignoring the bulk nucleation effect. On the other hand, the present model bases on the pressure difference $dp = P_{\text{sat}} - P^*$ evaluation and shows ability to reproduce better the behavior of flow. Figures 13 and 14 show a good level of agreement, in terms of radial vapor profile at $x = 0.59$ m, between present model and measurement. Among the models proposed by Janet et al. [24], results still show underprediction compared to experimental data.

To better predict local behaviors, the model should include the effects of bubble dynamics such as nuclei transport, break-up of bubbles, and influence of phase change into momentum and energy conservation equations. Besides, interphase momentum transfers between vapor and water phases in terms of drag, lift, wall lubrication, virtual mass, and turbulent dispersion force should be included to increase the accuracy of the model, as in Refs. [24] and [43]. Nondrag forces significantly influence the radial void fraction distribution, while lift force is a function of a bubble critical diameter (with change of sign) and becomes substantial for determining the shape of the void fraction. Finally, the wall force drives the bubbles away from the wall.

7 Conclusions, Outcomes, and Outlooks

In this study, a pressure-driven phase change model for flashing flows has been proposed. The model, implemented in the finite volume commercial solver ANSYS-FLUENT rel.16.2, is based on the two-phase mixture approach, including the slip effect and the boiling delay effect (viz. thermal nonequilibrium). The model has been validated by using the available experimental data of a convergent-divergent nozzle fed with subcooled water.

The comparison between numerical and experimental results shows a good level of agreement in terms of (a) mass flow rate (e.g., maximum relative error below 6%), (b) average vapor fraction, and (c) static pressure along the nozzle. Furthermore, the use of a pressure-driven phase change model permits us to better reproduce the turbulence effects and the radial vapor fraction profiles along the nozzle, compared with the temperature-driven models previously proposed in the literature. In addition, numerous sensitivity analyses have been performed (concerning RANS models, inlet turbulence boundary conditions, and artificial parameters) to provide practical guidelines. The main conclusions are: (a) turbulence model with standard wall function exhibits the best accuracy in terms of mass flow rate and vapor profile in combination with a suggested value of 1% for the inlet turbulence intensity; (b) the accommodation coefficient and the difference between saturation pressure and vapor partial pressure at the interface influence the numerical result and a suitable range of values is proposed for them.

Generally, the numerical results have shown an improvement compared to the previous works, for both global and local flow quantities. However, discrepancies have been observed between the experimental and numerical radial vapor profiles, possibly owing to the simplicity of the applied two-phase approach. In this respect, to improve the modeling of the local flow quantities in future works, an Euler multifluid approach (with a comprehensive set of nondrag forces) should be considered, along with a complete modeling of the thermal and nucleation effects present in the flashing process.

Nomenclature

$\mathbf{a}$ = acceleration vector (ms^{-2})
A = interfacial area density (m^{-1})
c = mass fraction
d = diameter of the particles (or droplets or bubbles) (m)
E = internal energy ($\mathrm{kg/m^2s^{-1}}$)
f = drag function
F = evaporation-condensation flux at flat interface ($\mathrm{kg/m^{-2}\,s^{-1}}$)
k = turbulence kinetic energy ($\mathrm{m^2s^{-2}}$)
L = the latent heat (J/kg)
M = molar mass (kg/kmol)
$\dot{m}$ = rate of mass transfer ($\mathrm{kg/m^{-3}s^{-1}}$)
n = number of phases
N = bubble number density
p = pressure (Pa)
p^* = vapor partial pressure at the interface on the vapor side (Pa)
R = gas constant R (KJ/KmolK)
Re = Reynolds number
Re = relative Reynolds number
t = time coordinate (s)
T = temperature (K)
$\mathbf{v}$ = velocity vector (ms^{-1})
x = x-coordinate (m)
y = y-coordinate (m)
y^+ = turbulence parameter

Greek Symbols

α = vapor volume fraction
β = accommodation coefficient
ε = turbulence dissipation rate ($\mathrm{m^2s^{-3}}$)
λ = thermal conductivity ($\mathrm{Wm^{-1}K^{-1}}$)
μ = dynamic viscosity (Pa·s)
ν_m = mixture turbulent viscosity ($\mathrm{m^2/s}$)
π = pi constant
ρ = density ($\mathrm{kg/m^{-3}}$)
σ_D = Prandtl dispersion coefficient (m)
τ = particle relaxation time (s)
ω = turbulence eddy frequency ($\mathrm{s^{-1}}$)

Subscripts

b = bubble
dr = drift
drag = drag
dr_x = axial component of drift velocity
dr_r = radial component of drift velocity
eff = effective
fi = flashing inception
i = interfacial
in = inlet
k = kth phase
l = liquid
m = mixture
p = secondary phase
q = primary phase
r = radial component
sat = saturation
t = turbulence
v = vapor
x = axial component

Appendix A: Sensitivity Analysis

In Appendix A, the influence of these coefficients to flashing flow has been displayed in Figs. 15–18 for cases (BNL284, BNL273, BNL268, and BNL304, respectively). A similar trend to case BNL309 in Fig. 7 is observed when varying coefficients.

Appendix B: Computational Cost

Computational cost to reach the full convergence is evaluated for case BNL309 using different turbulence models coupled with Standard Wall Function approach [62] and [78]. The criteria for convergence of numerical solution, required to be simultaneously satisfied, were defined as follows:

(i) Reduction of 10^{-6} in the numerical residual.
(ii) Relative error of mass flow rate between inlet and outlet below 1%.

Generally, all tested cases satisfy numerical convergence criteria at 8000 time steps with a time-step value at 10^{-5} and 10 iterations per time-step. Computational cost is provided in Table 13. All tested cases were run at a personal computer with four cores of Intel(R) Xeon(R) central processing unit E5670 @ 2.93 GHz 32 GB RAM.

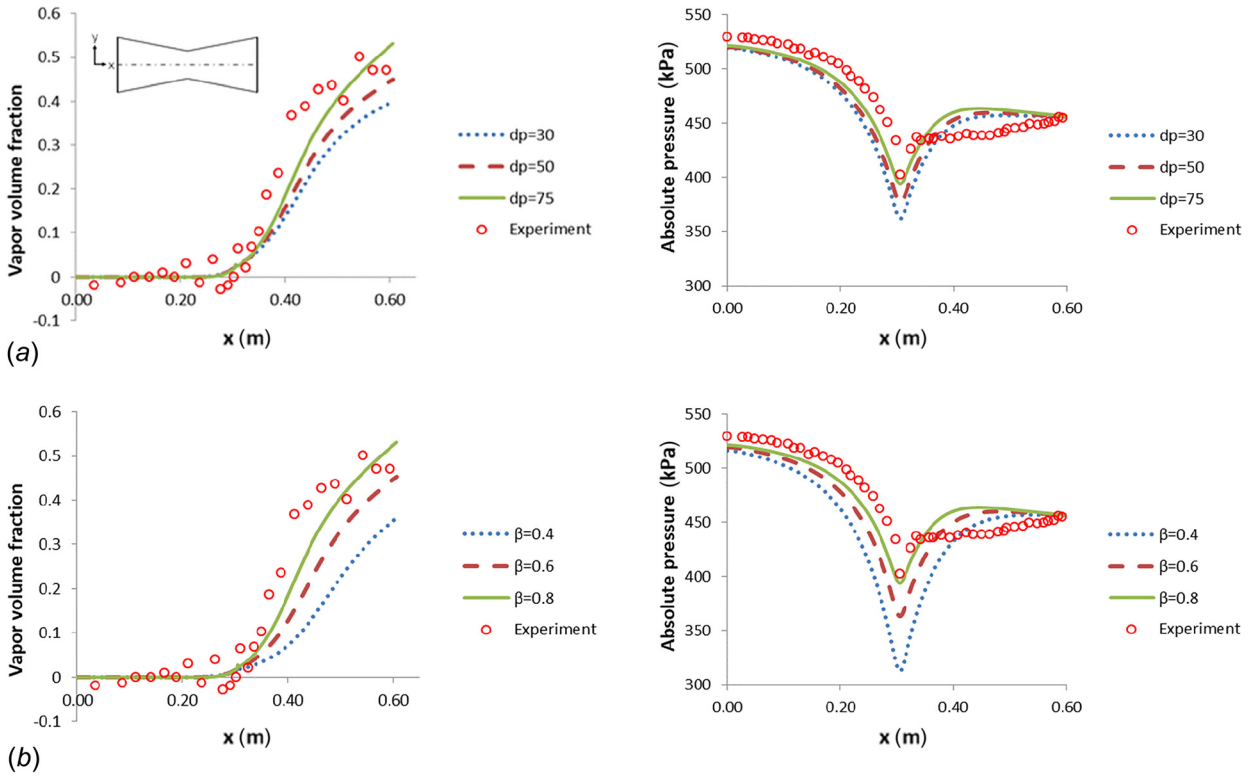

Fig. 15 Artificial coefficients sensitivity for BNL284: (*a*) vapor profile and static pressure along nozzle with fixed $d_p = 75$ Pa and (*b*) vapor profile and static pressure along nozzle with fixed $\beta = 0.8$

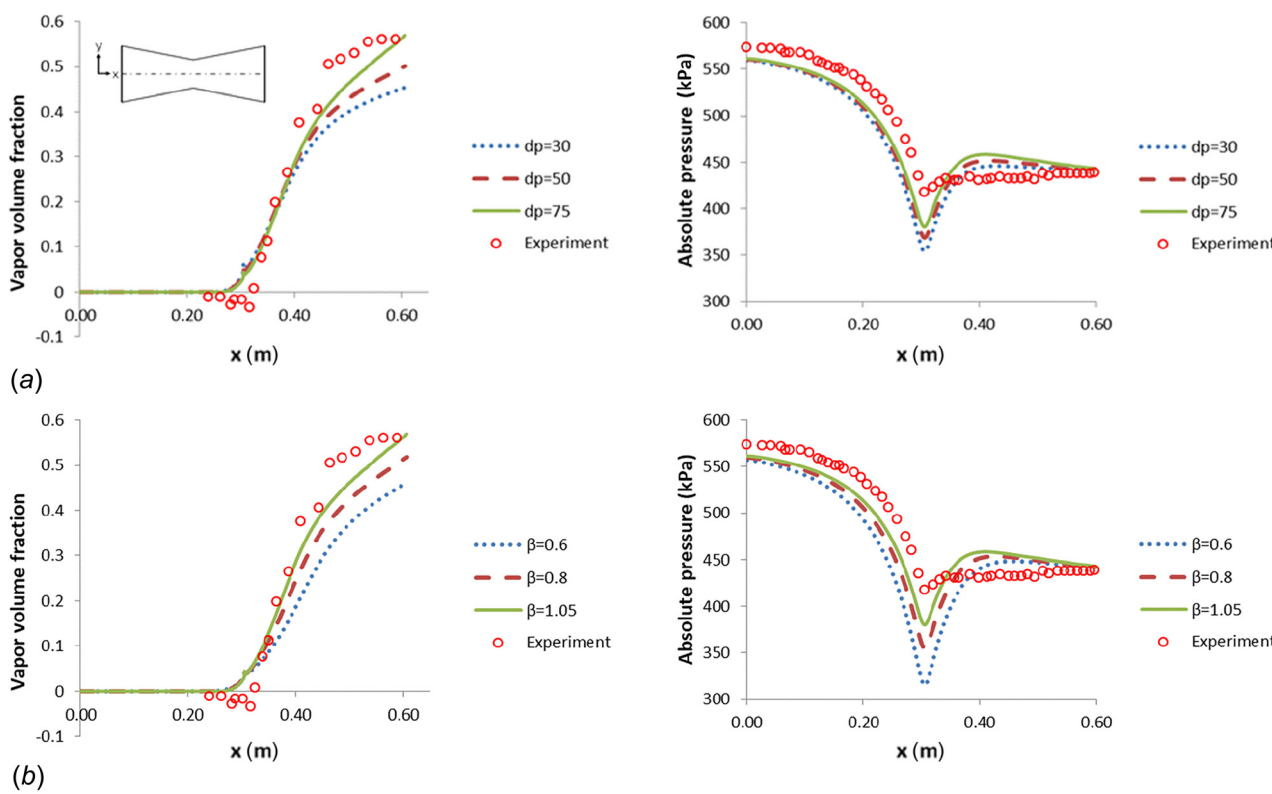

Fig. 16 Artificial coefficients sensitivity for BNL273: (*a*) vapor profile and static pressure along nozzle with fixed $d_p = 75$ Pa and (*b*) vapor profile and static pressure along nozzle with fixed $\beta = 1.05$

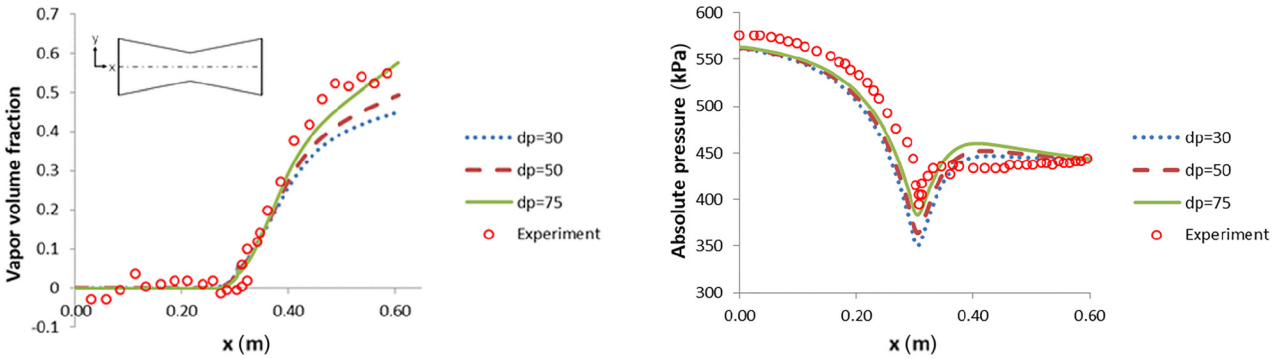

(*a*)

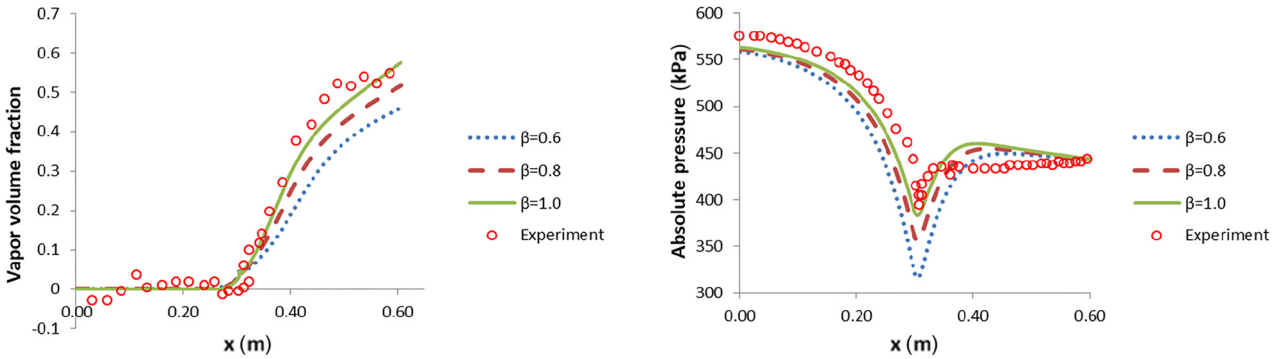

(*b*)

Fig. 17 Artificial coefficients sensitivity for BNL268: (*a*) vapor profile and static pressure along nozzle with fixed $d_p = 75$ Pa and (*b*) vapor profile and static pressure along nozzle with fixed $\beta = 1.0$

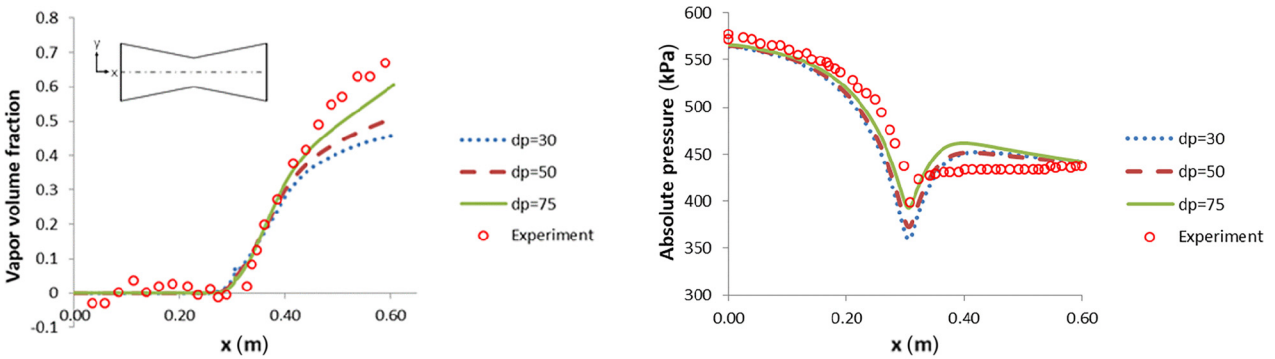

(*a*)

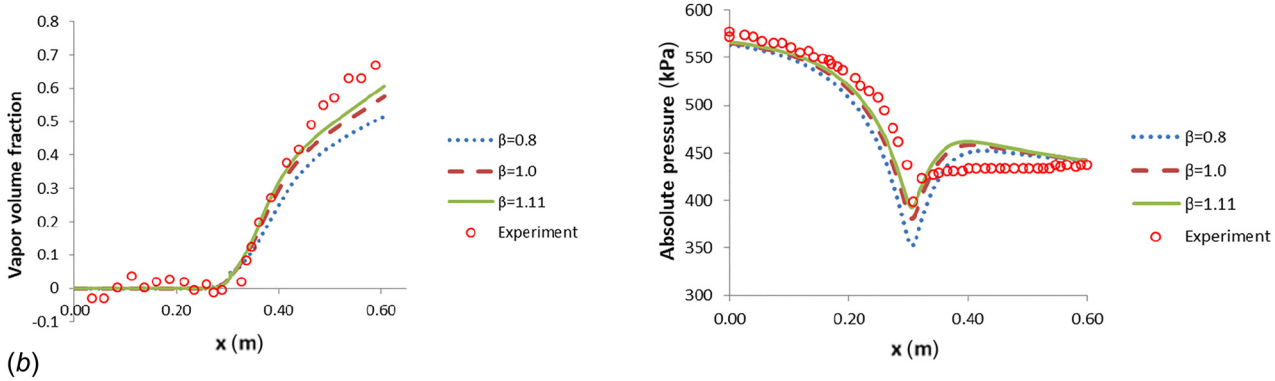

(*b*)

Fig. 18 Artificial coefficients sensitivity for BNL304: : (*a*) vapor profile and static pressure along nozzle with fixed $d_p = 75$ Pa and (*b*) vapor profile and static pressure along nozzle with fixed $\beta = 1.11$

Table 13 Computational cost corresponding to turbulence models

Cases	k–ω SST	Standard k–ω	Standard$k$–ϵ	Realizable k–ϵ	RNG k–ϵ	RSM
CPU time (s)	1	1.23	1.26	0.82	1.43	1.07
Δ [CPU time] (%)[a]	—	19.1	20.6	−21.5	30.1	7.1

[a]Approximated as $\left([\text{RANS model}] - [k\text{–}\omega\ \text{SST}]\right)/[\text{RANS model}]$.

References

[1] Saha, P., 1978, *A Review of Two-Phase Steam–Water Critical Flow Models With Emphasis on Thermal Non-Equilibrium*, U.S. Nuclear Regulatory Commission, Washington, DC.

[2] Wallis, G. B., 1980, "Critical Two-Phase Flow," Int. J. Multiphase Flow, **6**(1–2), pp. 97–112.

[3] Richter, H. J., 1983, "Separated Two-Phase Flow Model: Application to Critical Two-Phase Flow," Int. J. Multiphase Flow, **9**(5), pp. 511–530.

[4] Pinhasi, G. A., Ullmann, A., and Dayan, A., 2005, "Modeling of Flashing Two-Phase Flow," Rev. Chem. Eng., **21**(3–4), pp. 133–264.

[5] Xi, X., Liu, H., Jia, M., Xie, M., and Yin, H., 2017, "A New Flash Boiling Model for Single Droplet," Int. J. Heat Mass Transfer, **107**, pp. 1129–1137.

[6] Reocreux, M., 1978, "Contribution to the Study of Critical Flow Rates in Two-phase Water Vapour Flow," Ph.D. thesis, Scientific and Medical University of Grenoble, Grenoble, France.

[7] Schrock, V. E., Starkman, E. S., and Brown, R. A., 1977, "Flashing Flow of Initially Subcooled Water in Convergent-Divergent Nozzles," ASME J. Heat Transfer, **99**(2), pp. 263–268.

[8] Abuaf, N., 1981, *A Study of Nonequilibrium Flashing of Water in a Converging-Diverging Nozzle: Volume 1, Experimental*, U.S. Nuclear Regulatory Commission, Washington, DC.

[9] Araneo, L., and Donde', R., 2017, "Flash Boiling in a Multihole G-DI Injector—Effects of the Fuel Distillation Curve," Fuel., **191**, pp. 500–510.

[10] Henry, R. E., Fauske, H. K., and McComas, S. T., 1970, "Two-Phase Critical Flow at Low Qualities—II: Analysis," Nucl. Sci. Eng., **41**(1), pp. 92–98.

[11] Ishii, M., 1975, *Thermo-Fluid Dynamics Theory of Two-Phase Flow*, Eyrolles, Paris, France.

[12] Bouré, J. A., 1977, "The Critical Flow Phenomenon With Reference to Two-Phase Flow and Nuclear Reactor Systems," Winter Annual Meeting of the American Society of Mechanical Engineers, Atlanta, GA, Nov. 27–Dec. 2, pp. 195–216.

[13] Wendroff, B., 1979, "Two-Fluid Models: A Critical Study," EPRI Workshop on Two-Phase Flow, Tampa, FL, Mar. 2.

[14] Maksic, S., and Mewes, D., 2002, "CFD-Calculation of the Flashing Flow in Pipes and Nozzles," ASME Paper No. FEDSM2002-31033.

[15] Jones, O. C., and Zuber, N., 1978, "Bubble Growth in Variable Pressure Fields," ASME J. Heat Transfer, **100**(3), pp. 453–459.

[16] Shin, T. S., and Jones, O. C., 1986, "An Active Cavity Model for Flashing," Nucl. Eng. Des., **95**, pp. 185–196.

[17] Shin, T. S., and Jones, O. C., 1993, "Nucleation and Flashing in Nozzles—1," Int. J. Multiphase Flow, **19**(6), pp. 943–964.

[18] Blinkov, V. N., Jones, O. C., and Nigmatulin, B. I., 1993, "Nucleation and Flashing in Nozzles—2," Int. J. Multiphase Flow, **19**(6), pp. 965–986.

[19] Marsh, C. A., and O'Mahony, A. P., 2009, "Three-Dimensional Modelling of Industrial Flashing Flows," CFD2008, Trondheim, Norway, June 10–12.

[20] Blander, M., and Katz, J. L., 1975, "Bubble Nucleation in Liquids," AIChE J., **21**(5), pp. 833–848.

[21] Mimouni, S., Boucker, M., Lavieville, J., and Bestion, D., 2008, "Modelling and Computation of Cavitation and Boiling Bubbly Flows With the NEPTUNE CFD Code," Nucl. Eng. Des., **238**(3), pp. 680–692.

[22] Robert, M., Farvacque, M., Parent, M., and Faydide, B., 2003, "CATHARE 2 V2.5: A Fully Validated CATHARE Version for Various Application," Tenth International Topical Meeting on Nuclear Reactor Thermal-Hydraulics (NURETH 10), Seoul, South Korea, Oct. 5–11, p. 17.

[23] Archer, A., 2002, "A Predictive Model for Cavitation Erosion Downstream Orifices," ASME Paper No. FEDSM2002-31012.

[24] Janet, J. P., Liao, Y. X., and Lucas, D., 2015, "Heterogeneous Nucleation in CFD Simulation of Flashing Flows in Converging-Diverging Nozzles," Int. J. Multiphase Flow, **74**, pp. 106–117.

[25] Lemmert, M., and Chawla, J., 1977, "Influence of Flow Velocity on Surface Boiling Heat Transfer Coefficient," Heat Transfer Boil, **237**, p. 247.

[26] Kurul, N., and Podowski, M., 1991, "On the Modeling of Multidimensional Effects in Boiling Channels," ANS 27th National Heat Transfer Conference, Minneapolis, MN, July 28–31, pp. 28–31.

[27] Cole, R., 1967, "Bubble Frequencies and Departure Volumes at Subatmospheric Pressures," AIChE J., **13**(4), pp. 779–783.

[28] Kocamustafaogullari, G., and Ishii, M., 1983, "Interfacial Area and Nucleation Site Density in Boiling Systems," Int. J. Heat Mass Transfer, **26**(9), pp. 1377–1387.

[29] Riznic, J., and Ishii, M., 1989, "Bubble Number Density in Vapor Generation and Flashing Flow," Int. J. Heat Mass Transfer, **32**(10), pp. 1821–1833.

[30] Rohatgi, U., and Reshotko, E., 1975, "Non-Equilibrium One-Dimensional Two-Phase Flow in Variable Area Channels," Winter Annual Meeting, Houston, TX, Nov. 30–Dec. 5, pp. 47–54.

[31] Wu, B., Saha, P., and Abuaf, N., 1981, *A Study of Nonequilibrium Flashing of Water in a Converging–Diverging Nozzle*, Vol. 2, NUREG/CR.U.S.N.R.C., Commission, U.N.R., Washington, DC.

[32] Pelletingeas, A., Dufresne, L., and Seers, P., 2016, "Characterization of Flow Structures in a Diesel Injector for Different Needle Lifts and a Fluctuating Injection Pressure," ASME J. Fluids Eng., **138**(8), p. 081105.

[33] Giese, T., Lauren, E., and Schwarz, W., 2002, "Experimental and Numerical Investigation of Gravity-Driven Pipe Flow With Cavitation," ASME Paper No. ICONE10-22026.

[34] Laurien, E., and Giese, T., 2003, "Exploration of the Two-Fluid Model of Two-Phase flow Towards Boiling, Cavitation and Stratification," Third International Conference on Computational Heat and Mass Transfer (ICCHMT), Banff, AB, Canada, May 26–30.

[35] Laurien, E., 2004, "Influence of the Model Bubble Diameter on Three-Dimensional Numerical Simulations of Thermal Cavitation in Pipe Elbows," Third International Symposium on Two-Phase Modelling and Experimentation, Pisa, Italy, Sept. 22–25, pp. IV-2113-2120.

[36] Frank, T., 2007, "Simulation of Flashing and Steam Condensation in Subcooled Liquid Using ANSYS CFX," Fifth FZD & ANSYS MPF Workshop, Dresden, Germany, Apr. 25–27, pp. 1–29.

[37] Liao, Y., Lucas, D., Krepper, E., and Rzehak, R., 2013, "Flashing Evaporation Under Different Pressure Level," Nucl. Eng. Des., **265**, pp. 801–813.

[38] Schaffrath, A., Krüssenberg, A.-K., Weiß, F.-P., Hicken, E. F., Beyer, M., Carl, H., Prasser, H.-M., Schuster, J., Schütz, P., and Tamme, M., 2001, "TOPFLOW—A New Multipurpose Thermal Hydraulic Test Facility for the Investigation of Steady State and Transient Two-Phase Flow Phenomena," Kerntechnik, **66**, pp. 209–212.

[39] Yazdani, M., Alahyari, A. A., and Dradcliff, T. D., 2013, "Numerical Modeling and Validation of Supersonic Two-Phase Flow of CO_2 in Converging-Diverging Nozzles," ASME J. Fluids Eng., **136**(1), p. 014503.

[40] Singhal, A. K., Athavale, M. M., Li, H., and Jiang, Y., 2002, "Mathematical Basis and Validation of the Full Cavitation Model," ASME J. Fluids Eng., **124**(3), pp. 617–624.

[41] Brennen, C. E., 2005, *Fundamentals of Multiphase Flow*, Cambridge University Press, Cambridge, UK.

[42] Nakagawa, M., Berana, M. S., and Kishine, A., 2009, "Supersonic Two-Phase Flow of CO_2 Through Converging-Diverging Nozzles for the Ejector Refrigeration Cycles," Int. J. Refrig., **32**(6), pp. 1195–1202.

[43] Liao, Y., and Lucas, D., 2015, "3D CFD Simulation of Flashing Flows in a Converging-Diverging Nozzle," Nucl. Eng. Des., **292**, pp. 149–163.

[44] Liao, Y., and Lucas, D., 2017, "Possibilities and Limitations of CFD Simulation for Flashing Flow Scenarios in Nuclear Applications," Energies, **10**(1), p. 139.

[45] Jin, M. S., Ha, C. T., and Park, W. G., 2017, "Numerical Study on Heat Transfer Effects of Cavitating and Flashing Flows Based on Homogeneous Mixture Model," Int. J. Heat Mass Transfer, **109**, pp. 1068–1083.

[46] Ha, C. T., Park, W. G., and Merkle, C. L., 2009, "Multiphase Flow Analysis of Cylinder Using a New Cavitation Model," Seventh International Symposium on Cavitation, Ann Arbor, MI, Aug. 16–20.

[47] Manninen, M., Taivassalo, V., and Kallio, S., 1996, "On the Mixture Model for Multiphase Flow," VTT Publications 288, Technical Research Center of Finland, Finland.

[48] Zuber, N., and Findlay, J. A., 1965, "Average Volumetric Concentration in Two-Phase Flow Systems," ASME J. Heat Transfer, **87**(4), pp. 453–468.

[49] Pericleous, K. A., and Drake, S. N., 1986, *An Algebraic Slip Model of Phoenics for Multi-Phase Applications, Numerical Simulation of Fluid Flow and Heat/Mass Transfer Processes*, Springer-Verlag, Berlin.

[50] Verloop, W. C., 1995, "The Inertial Coupling Force," Int. J. Multiphase Flow, **21**(5), pp. 929–933.

[51] Ungarish, M., 1993, *Hydrodynamics of Suspensions: Fundamentals of Centrifugal and Gravity Separation*, Springer, Berlin.

[52] Johansen, S. T., Anderson, N. M., and De Silva, S. R., 1990, "A Two-Phase Model for Particle Local Equilibrium Applied to Air Classification of Powers," Power Technol., **63**(2), pp. 121–132.

[53] Morgan, M. J., and Shapiro, H. N., 2006, *Fundamentals of Engineering Thermodynamics*, Wiley, London.

[54] Miyatake, O., Tanaka, I., and Lior, N., 1997, "A Simple Universal Equation for Bubble Growth in Pure Liquids and Binary Solutions With a Non-Volatile Solute," Int. J. Heat Mass Transfer, **40**(7), pp. 1577–1584.

[55] Oza, R. D., and Sinnamon, J. F., 1983, "An Experimental and Analytical Study of Flashing Boiling Fuel Injection," SAE Paper No. 830590.

[56] Barbone, R., 1994, "Explosive Boiling of a Depressurized Volatile Liquid," M.Sc. thesis, McGill University, Montreal, QC, Canada.

[57] Sher, E., Bar-Kohany, T., and Rashkovan, A., 2008, "Flash-Boiling Atomization," Prog. Energy Combust. Sci., **34**(4), pp. 417–439.

[58] ANSYS, 2016, "User's Guide of ANSYS-FLUENT 16.2," ANSYS Inc., Canonsburg, PA.

[59] Naumann, Z., and Schiller, L., 1935, "A Drag Coefficient Correlation," Z. Ver. Dtsch. Ing., **77**(3), pp. 318–323.
[60] Lee, W. H., 1980, "A Pressure Iteration Scheme for Two-Phase Flow Modeling," *Multi-Phase Transport Fundamentals*, Hemisphere Publishing, Washington, DC.
[61] Hinze, J. O., 1975, *Turbulence*, 2nd ed., McGraw-Hill, New York.
[62] Colombo, E., Inzoli, F., and Mereu, R., 2012, "A Methodology for Qualifying Industrial CFD: The Q^3 Approach and the Role of a Protocol," Comput. Fluids, **54**, pp. 56–66.
[63] Launder, B. E., and Spalding, D. B., 1972, *Lectures in Mathematical Models of Turbulence*, Academic Press, London.
[64] Shih, T.-H., Liou, W. W., Shabbir, A., Yang, Z., and Zhu, J., 1995, "A New $k-\varepsilon$ Eddy-Viscosity Model for High Reynolds Number Turbulent Flows—Model Development and Validation," Comput. Fluids, **24**(3), pp. 227–238.
[65] Yakhot, V., Orszag, S. A., Thangam, S., Gatski, T. B., and Speziale, C. G., 1992, "Development of Turbulence Models for Shear Flows by a Double Expansion Technique," Phys. Fluids A, **4**(7), pp. 1510–1520.
[66] Launder, B. E., Reece, G. J., and Rodi, W., 1975, "Progress in the Development of a Reynolds-Stress Turbulence Closure," J. Fluid Mech., **68**(3), pp. 537–566.
[67] Wilcox, D. C., 1988, "Reassessment of the Scale-Determining Equation for Advanced, Turbulence Models," AIAA J., **26**(11), pp. 1299–1310.
[68] Wilcox, D. C., 1993, "Comparison of Two-Equation Turbulence Models for Boundary Layers With Pressure Gradients," AIAA J., **31**(8), pp. 1414–1421.
[69] Wilcox, D. C., 1993b, *Turbulence Modelling for CFD*, DCW Industries, La Canada, CA.
[70] Wilcox, D. C., 1994, "Simulating Transition With a Two-Equation Turbulence Model," AIAA J., **32**(2), pp. 247–255.
[71] Menter, F. R., 1992, "Performance of Popular Turbulence Models for Attached and Separated Adverse Pressure Gradient Flow," AIAA J., **30**(8), pp. 2066–2072.
[72] Menter, F. R., 1992, "Improved Two-Equation k–ω Turbulence Models for Aerodynamic Flows," Ames Research Center, Mountain View, CA, NASA Technical Memorandum No. 103975.
[73] Menter, F., 1994, "Two-Equation Eddy-Viscosity Turbulence Model for Engineering Applications," AIAA J., **32**(8), pp. 1598–1605.
[74] Menter, F. R., Kuntz, M., and Langtry, R., 2003, "Ten Years of Industrial Experience With the SST Turbulence Model," Fourth International Symposium on Turbulence, Heat and Mass Transfer, Antalya, Turkey, Oct. 12–17.
[75] Launder, B. E., and Spalding, D. B., 1974, "The Numerical Computation of Turbulent Flows," Comput. Methods Appl. Mech. Eng., **3**(2), pp. 269–289.
[76] Kim, S.-E., and Choudhury, D., 1995, "A Near-Wall Treatment Using Wall Functions Sensitized to Pressure Gradient," Symposium on Fluids Engineering and Laser Anemometry Conference, Separated and complex flows, Hilton Head, SC, pp. 273–280.
[77] Besagni, G., and Inzoli, F., 2017, "Computational Fluid-Dynamics Modeling of Supersonic Ejectors: Screening of Turbulence Modeling Approaches," Appl. Therm. Eng., **117**, pp. 122–144.
[78] Besagni, G., Mereu, R., Chiesa, P., and Inzoli, F., 2015, "An Integrated Lumped Parameter-CFD Approach for Off-Design Ejector Performance Evaluation," Energy Convers Manage, **105**, pp. 697–715.
[79] Roache, P. J., 1998, *Verification and Validation in Computational Science and Engineering*, *Albuquerque*, Hermosa Publishers, Socorro, NM.